Fourier-Space Image Reconstruction Using Microwave Measurements

Reza K. Amineh and *Natalia K. Nikolova*

The use of electromagnetic waves at microwave and millimeter-wave (mm-wave) frequencies in imaging has been growing rapidly in the last two decades with applications in security screening, biomedical imaging, nondestructive testing, and the inspection of goods and packages. The nonionizing nature of the radiation renders microwave and mm-wave imaging (MMI) safe for humans and, thus, attractive, especially for frequent imaging of living tissue and humans. At the same time, the radiation penetrates many materials, which are optically opaque: e.g., fog and foliage, soil and living tissue, brick and drywall, wood, fabrics, and plastics. Importantly, modern MMI systems offer compact and relatively low-cost hardware due to advancements in high-frequency microelectronics.

Several categories of image reconstruction methods have been developed so far for the MMI systems, mainly including optimization-based techniques, time-domain synthetic aperture radar, and back-projection techniques, as well as frequency-domain holographic techniques. Compared to the optimization-based techniques, holographic techniques offer much higher image reconstruction speed and robustness to noise and interference. While originally holographic imaging was only capable of providing fast qualitative images, like time-domain radar-based imaging, recently this shortcoming has been addressed by fast quantitative holographic imaging techniques. Currently, holographic techniques can provide qualitative or quantitative images of large objects (e.g., a person) within seconds using regular computers. The processing involves Fourier transform (FT) and inverse FT, which are implemented efficiently by fast FT (FFT) algorithms. The speed and resilience to noise and measurement uncertainty have made microwave holography the preferred image-reconstruction method in commercial whole-body imagers (found in major airports worldwide) and, more recently, in biomedical and nondestructive-testing imaging.

In the early stages, when intensity (or power) measurements only were available, microwave holography closely resembled optical holography. Later, synthetic aperture radar (SAR) processing techniques were employed to take advantage of the availability of

Reza K. Amineh (rkhalaja@nyit.edu) is with the Department of Electrical and Computer Engineering, New York Institute of Technology, New York, NY 10023 USA. Natalia K. Nikolova (talia@mcmaster.ca) is with the Department of Electrical and Computer Engineering, McMaster University, Hamilton, ON L8S 4K1, Canada.

Digital Object Identifier 10.1109/MMM.2024.3403047

Date of current version: 15 July 2024

©SHUTTERSTOCK.COM/AGSANDREW

complex-valued (magnitude and phase) microwave data. With measurements over rectangular or cylindrical apertures, 3D image reconstruction became possible. To this day, FFT-based image reconstruction remains the most computationally efficient option for reconstructing 3D images with millions of voxels within seconds.

Traditional SAR-based inversion strategies employ far-field approximations and point-wise antenna assumptions. Thus, when applied with extreme near-field measurements, such as those used in biomedical imaging and nondestructive testing, the images are often erroneous. To address this problem, near-field holographic MMI methods have been developed that are capable of processing even evanescent-field data resulting in high-resolution images. Further advancements include image reconstruction with bistatic measurements, both back-scattered and forward-scattered fields, as well as with multiple-input, multiple-output (MIMO) measurements. Common holographic methods work with stepped-frequency continuous wave (SFCW) data but they have also been extended to work with linear frequency modulation (LFM) radars.

Due to the rapid growth in the research and development of radar imaging technology, the literature abounds with articles about SAR-based imaging methods and the closely related methods of microwave holography. Yet, the subject is scattered across many disciplines and the commonality of principles is often lost, hampering understanding and appreciation of the methods' differences and their limitations. In this article, we aim to provide a streamlined overview of the Fourier-based methods for microwave and mm-wave image reconstruction, a discussion of their limitations, and some illustrative examples of recent applications. This review is far from being comprehensive or complete, as the subject is developing at a very fast pace: Since 2022, more than 5,600 articles about SAR imaging have been published on the IEEE*Xplore*® platform alone. We hope that this article will benefit both experts and novices in the field of radar imaging. We have endeavored to make it not just a review but also a tutorial, providing a

common framework to compare and contrast the mathematical and implementational aspects of the modern MMI systems.

Early Developments

The origins of holographic imaging are attributed to Gabor [1], whose work (dating back to the late 1940s) aimed at improving electron microscopy by employing a clever two-step measurement procedure. In the first recording step, the object is illuminated with a focused electron beam. The resulting scattered wave is allowed to interfere with a copy of the illuminating beam (the reference wave) and the diffraction pattern resulting from this interference is recorded on a photographic plate. Gabor named this recording the *hologram*. The photographic hologram is then processed and scaled up to optical wavelengths. In a second reconstruction step, an optical illumination system is employed, which is a scaled-up copy of the electron-beam illumination system. Now the object is absent, but the processed hologram (a photograph) is placed in the same (but scaled) position relative to the wave source (now monochromatic light). Upon optical illumination, the wave emerging from the hologram is focused by a lens to produce a high-resolution optical replica of the object originally scanned by the electron beam. Further improvements to Gabor's setup were brought forward by Leith and Upatnieks [2], in which the availability of lasers led to a new generation of 3D imaging optical systems. A review of optical holography is available in [3].

The term *holography* has Greek origins, with the meaning of *holos* for "whole" and *graphe* for "writing." In instrumentation, holography is defined as an interferometric technique for recording the amplitude and the phase of monochromatic waves [4]. In imaging, holography refers to a class of image-reconstruction methods, which process complex-valued (amplitude and phase) data using 2D and/or 3D direct and inverse FTs. The direct FT maps the data dependence on the real-space variables (x, y, z) onto the wavenumber space, (k_x, k_y, k_z), or k-space, where the target reflectivity is computed. The inverse FT maps the reconstructed reflectivity from k-space back to real space.

Soon after the discovery of optical holography, its principles were translated to acoustics [5] for imaging objects hidden inside optically opaque media. Concurrently (in the mid-1960s), holography with microwaves emerged [6], which, too, aimed at imaging optically obscured objects. In those early stages, microwave holography was similar to its optical counterpart in its two-step procedure [7]. In a recording step, an intensity pattern (the hologram of the interfering scattered and reference waves) is measured by scanning an antenna equipped with a simple diode detector over the acquisition plane [8]. The microwave hologram is then scaled to optical frequencies and illumination by light reveals the microwave image of the object.

The later developments of holographic MMI, now widely employed in practice and in research, can be divided into four separate paths: 1) indirect holography for 2D image reconstruction (IH2D), 2) direct holography for 3D image reconstruction (DH3D) with far-field data, 3) direct holography for slice-by-slice 3D image reconstruction (DH3D-S) with far-field data, and 4) direct holography for 3D image reconstruction with near-field data (DH3D-N). While there are significant algorithmic differences between these categories, they share a few common features.

- They exploit the magnitude and the phase of the scattered waves.
- They provide images with enhanced resolution compared to the images obtained from raw measurements. As an example, Figure 1 shows the improvement achieved when imaging small metallic objects hidden inside wood. The objects' presence or location cannot be deduced from the raw magnitude and phase data plotted in Figure 1(a) and (b). But the processing with a holographic imaging algorithm provides the high-quality images in Figure 1(c) and 1(d).
- They employ a linearized model of electromagnetic scattering. This means that the interactions, such as mutual coupling and multiple scattering among the scatterers in the scene, are neglected. The object is viewed simply as a collection of independent point scatterers. This is the well-known Born approximation in imaging [9].
- They reconstruct the object in the wavenumber space (the k-space) with remarkable speed due to very low computational complexity compared to the real-space solutions of the inverse scattering problems [3].

IH2D

Indirect holography is a modern interferometric technique to extract the magnitude and phase of scattered-field data from intensity (scalar) measurements. Thus, as a data acquisition technique, it resembles optical holography. The intensity of the sum of the reference and scattered signals (both at a single frequency) is measured over an acquisition plane, providing a 2D dataset (a function of x and y), i.e., a hologram. Unlike optical holography, however, the reference signal is submitted to the receiver through a waveguide or a transmission line. Also, the image is obtained by processing the hologram data on a computer, unlike Gabor's reconstruction, which employs an optical reconstruction-step measurement with the hologram.

Figure 2 illustrates the modern indirect holography system employed in microwave imaging [10]. The imaged object is illuminated by a transmitting (TX) antenna. The scattered field due to the object $E^{sc}(x, y)$ is captured by a receiving (RX) antenna over a rectangular aperture at $\bar{z}$. The received signal, along with the phase-coherent reference signal $E^{ref}(x, y)$ (from a signal generator), are applied to the input ports of a hybrid tee. One of the outputs of the hybrid tee provides the sum of the two inputs, which is measured by a power meter (e.g., a diode detector). The other output port providing the difference of $E^{sc}(x, y)$ and $E^{ref}(x, y)$ is often terminated by a matched load, but it may also be recorded and employed to enhance the hologram processing [10].

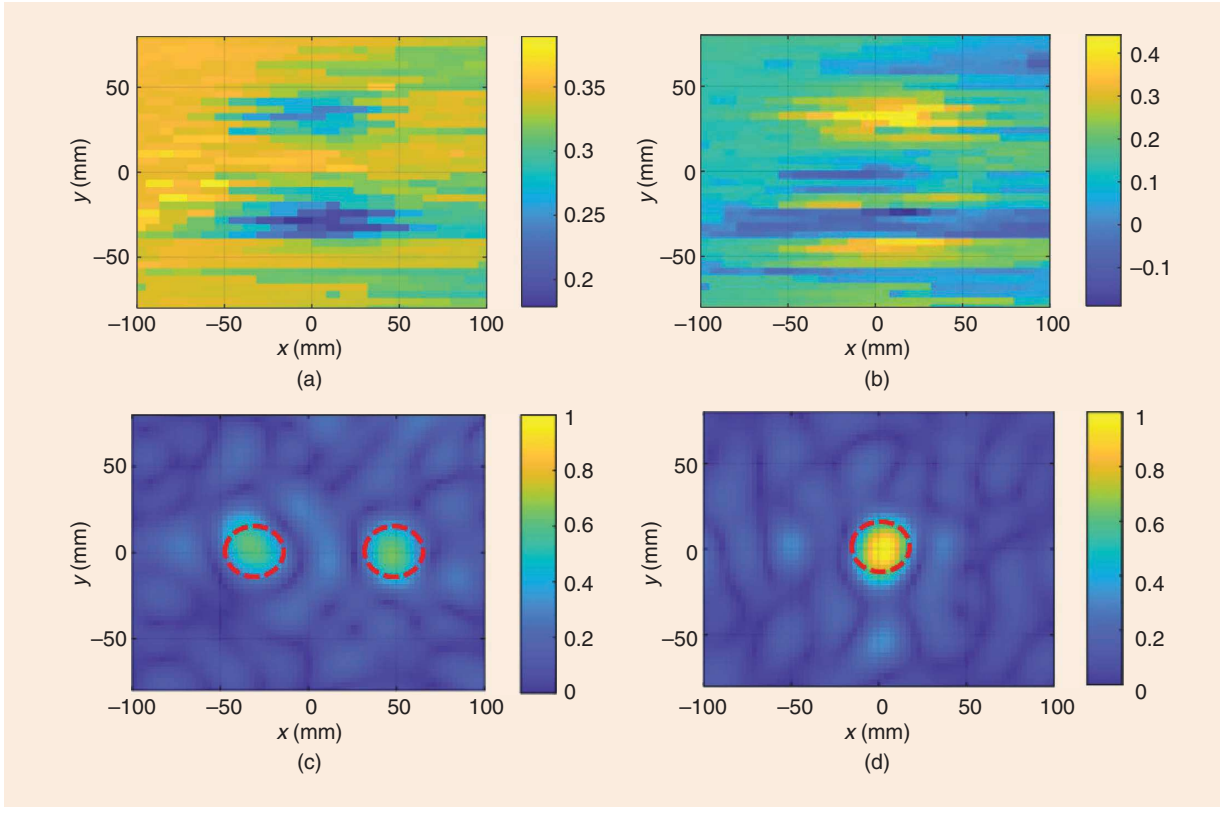

Figure 1. *Measured backscattered responses at 7 GHz over a 2D aperture obtained with metallic objects hidden inside wood and placed at 14 mm (two side-by-side objects) and 42 mm (single object) from the measured aperture: (a) magnitude and (b) phase (in radians). Holographic images using wideband data (2.8 to 11 GHz) of the objects at imaged planes located at two range distances: (c) 14 mm and (d) 42 mm. The red dashed lines show the actual position of the objects.*

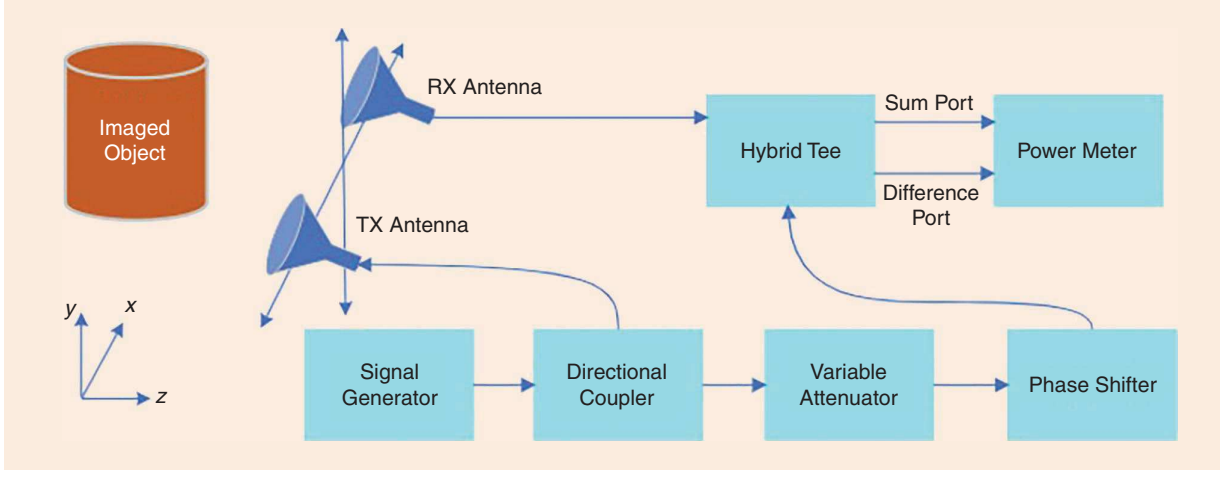

Figure 2. *Block diagram of an IH2D measurement system (modified from [10]). RX: receiving; TX: transmitting.*

The reference signal $E^{\text{ref}}(x, y)$ has a uniform amplitude E_0, but its phase is controlled by a phase shifter so that it decreases linearly along the scanned direction. For example, for a scan along x, an effective wavenumber $k_r = k_x$ is selected, and for every sampling step Δx, the reference-signal phase delay is incremented by $\Delta\phi = k_x \Delta x$. For a 2D scan along x and y, the reference signal is synthesized as $E^{\text{ref}}(x, y) = E_0 e^{-\text{i}k_x x - \text{i}k_y y}$, where E_0 is a constant magnitude. Thus, the reference signal emulates a plane wave of wavenumber $k_r = \sqrt{k_x^2 + k_y^2}$ with the wavenumbers along x and y being k_x and k_y, respectively.

The intensity pattern $I(x, y)$ recorded by the power meter at the sum port of the hybrid tee is expressed as [10]:

$$\begin{aligned} I(x, y) &= |E^{\text{sc}}(x, y) + E^{\text{ref}}(x, y)|^2 \\ &= |E^{\text{sc}}(x, y)|^2 + E_0^2 + 2E_0 \,\text{Re}\{E^{\text{sc}}(x,y) e^{\text{i}k_x x + \text{i}k_y y}\}. \end{aligned} \quad (1)$$

Further, the 2D FT of $I(x, y)$ is obtained:

$$\begin{aligned} \mathcal{F}_{2\text{D}}\{I(x, y)\} = \mathcal{F}_{2\text{D}}\{|E^{\text{sc}}(x, y)|^2\} + E_0^2 \delta(k_x, k_y) \\ + 2E_0 \mathcal{F}_{2\text{D}}\{\text{Re}[E^{\text{sc}}(x, y) e^{\text{i}k_x x + \text{i}k_y y}]\} \end{aligned} \quad (2)$$

where $\mathcal{F}_{2\text{D}}\{\cdot\}$ denotes the 2D FT. The first two terms in (2) are centered at the origin of k-space spanned by the variables k_x and k_y. On the other hand, the third term is the spectrum of the scattered field $\tilde{E}^{\text{sc}}(k_x, k_y)$ shifted away from the origin by $k_r = \sqrt{k_x^2 + k_y^2}$. With far-field reflection measurements, the spectrum of the scattered field contains only propagating modes and is thus limited within the maximum wavenumber $k_{\text{max}} \approx 2k$, where k is the wavenumber of the radiation in the background medium (e.g., air) [3]. As long as k_r is chosen large enough to satisfy $k_r > 3k_{\text{max}}$, the spectral content of the third term in (2) can be separated by high-pass filtering. Figure 3 illustrates the separation of the first two terms in (2) from the third term through a cut along the k_x axis. After separating the desired scattered-field spectrum using high-pass filtering, the result is synthetically shifted to the center of k-space by removing the known wavenumber shift (k_x, k_y). Applying inverse FT to the result retrieves the complex-valued scattered field $E^{\text{sc}}(x, y)$, which is then processed with any available reconstruction algorithm to produce a 2D image of the object. In [10], a back-propagation algorithm (BPA) is used.

The IH2D imaging method has been employed to perform preliminary experiments for breast-cancer imaging [11] and the imaging of metallic objects [12]. Despite offering simple and low-cost data acquisition (due to scalar measurements only), a major limitation is that the data acquisition employs single-frequency radiation, which is not sufficient for 3D imaging. This is the likely reason for the method not being as widely deployed in imaging as the 3D direct microwave holography techniques discussed next.

DH3D With Far-Field Measurements

The direct holographic MMI methods use more complicated measurement hardware (e.g., vector network analyzers) to obtain the magnitude and phase of the scattered responses. Both SFCW and LFM measurements can be processed by DH3D. If wideband time-domain measurements are used, they are converted to frequency-dependent signals via FT before they are processed by DH3D.

Similar to IH2D, the measurements are performed over an aperture of canonical shape (e.g., rectangular or cylindrical). DH3D has been inspired by the early 2D SAR imaging approaches and, on a fundamental level, it can be viewed as their extension to 3D imaging. SAR utilizes wideband radar data acquired over a line [13]. The data span 2D space (the position x along the line and time t, or frequency ω). The image reconstruction maps the data onto a 2D reflectivity image of the target along the cross-range x and range z. In contrast, DH3D takes wideband data on a 2D surface. Now the data span a 3D space (the position coordinates x and y,

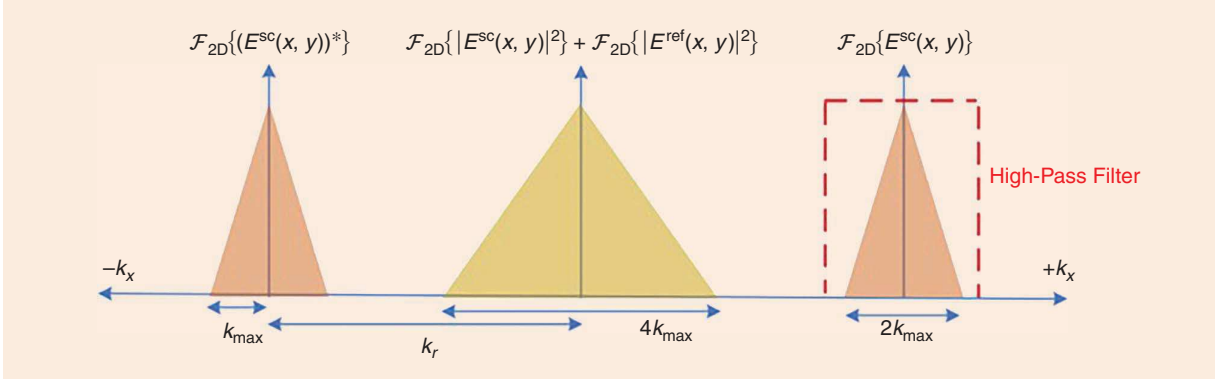

Figure 3. *The cross-section (along the k_x axis) of the spatial-frequency spectrum of the intensity pattern recorded at the sum port of the hybrid tee in the IH2D acquisition method (modified from [10]).*

and time t, or frequency ω). This enables the 3D image reconstruction in x, y, and z.

The first attempts to extend 2D SAR to 3D imaging date back to the 1990s [14], [15], [16]. The method proposed in [16] extends the projection (also known as *back-propagation*) image-reconstruction algorithm, common in SAR, to 3D imaging by the use of the range migration algorithm (RMA), which provides the link between the frequency (ω) dependence of the data and the range (or depth) dependence of the image. The resulting 3D image reconstruction method is known as ω–k *SAR* [17]. Only a few years earlier, the team at the Pacific Northwest National Laboratory pioneered a robust method for security screening [14], [15], exploiting a range-migration principle, which is mathematically equivalent to the RMA. They refer to their method as *wideband microwave holography* in recognition of the fact that it can be viewed as an extension of the early single-frequency 2D microwave-holography imaging to wideband operation with 3D imaging output.

Most applications envision monostatic measurements of objects residing in the far zone of the TX/RX antennas. In such measurements, the TX and RX antennas occupy the same position. Figure 4 illustrates the monostatic arrangement with a planar scan, where the acquisition plane is at $z = \bar{z}$, the measurements' coordinates are $\boldsymbol{r} = (x, y, \bar{z})$, and the coordinates in the imaged volume are $\boldsymbol{r}' = (x', y', z')$. We use this relatively simple scenario to explain the principle of DH3D imaging.

DH3D employs analytical models of the scattered field due to a point scatterer in a homogeneous background. The central role in the model is played by the function $H(\boldsymbol{r} - \boldsymbol{r}', \omega)$, which is referred to as the *system* (*or data*) *point-spread function* (*PSF*). It predicts what the scanning system would measure at $\boldsymbol{r}$ when the scattering originates from a point at $\boldsymbol{r}'$. The term *PSF* is attributed to the fact that while the scattering source is a point, its scattered field, when measured at the aperture, is spread over a substantial area. Mathematically, $H(\boldsymbol{r} - \boldsymbol{r}', \omega)$ can also be viewed as the system spatial impulse response. It is the assumption of a homogeneous background that allows the PSF dependence on $\boldsymbol{r}$ and $\boldsymbol{r}'$ to appear as $(\boldsymbol{r} - \boldsymbol{r}')$. This dependence is critical for the ability to carry out the image reconstruction efficiently in k-space.

Imaging with planar scans employs a Cartesian coordinate system, where the PSF is written as $H(x - x', y - y', \bar{z} - z', \omega)$. Table 1 summarizes the analytical PSFs used by all far-field image-reconstruction methods, DH3D included, for the case of monostatic measurements. Note that the functions in the first column of Table 1 are given in a form, which assumes that the scattering point is at the origin, $x' = y' = z' = 0$, whereas the measurement point is at (x, y, z). If the scattering point is not at the origin, a simple coordinate shift in the form of $H(x - x', y - y', \bar{z} - z', \omega)$, models properly the PSF observed at (x, y, z), provided the background is homogeneous. The respective 2D FTs are listed in the second column of Table 1, since they are used in the fast 3D image reconstruction in k-space. The 2D FT is applied to the lateral (cross-range) coordinates (x, y) producing $\tilde{H}(k_x, k_y, z, \omega)$, where k_x and k_y are the Fourier variables.

We notice that all three PSFs in Table 1 account for the phase delay associated with the signal path length from the TX antenna to the point scatterer and back to the RX antenna. On the other hand, not all three PSFs represent the spherical-spread loss (i.e., the free-space path loss) of the incident and scattered waves. The PSF in the first row in Table 1 ignores the waves'

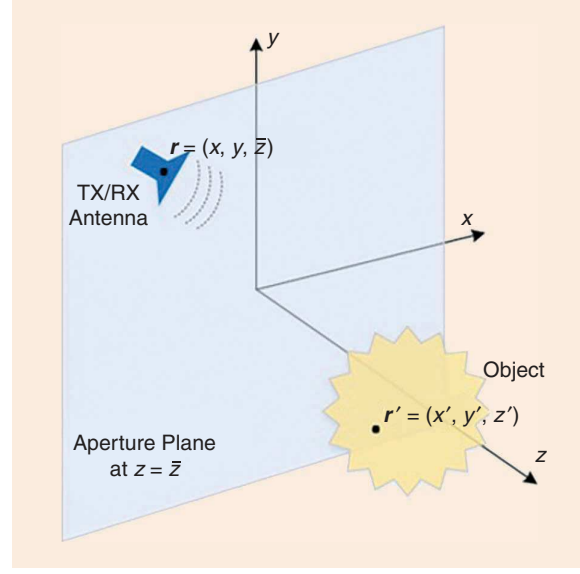

Figure 4. *Illustration of the DH3D monostatic system. Measurements of the wideband back-scattered waves are performed over the rectangular aperture at $z = \bar{z}$ and 3D images of the object can be reconstructed practically instantaneously using the technique in [15].*

TABLE 1. Analytical system PSFs used in far-field imaging with monostatic radar and their 2D Fourier transforms.

Real Space: $H(x, y, z, \omega)$	2D Fourier Space: $\tilde{H}(k_x, k_y, z, \omega)$	Source
$e^{-i2k(\omega)r}$	$\sim e^{-ik_z(\omega)\lvert z\rvert}, \sim \frac{i2\pi k(\omega)}{k_z^2(\omega)} e^{-ik_z(\omega)\lvert z\rvert}$	[15], [16]
$\frac{e^{-i2k(\omega)r}}{r}$	$\frac{i2\pi}{k_z(\omega)} e^{-ik_z(\omega)\lvert z\rvert}$	[18], [19]
$\frac{e^{-i2k(\omega)r}}{r^2}$	$\frac{\pi}{ik(\omega)\lvert z\rvert} e^{-ik_z(\omega)\lvert z\rvert}$	[20]
$r = \sqrt{x^2 + y^2 + z^2}$	$k_z = \sqrt{(2k)^2 - k_x^2 - k_y^2} \geq 0,$ $k_x, k_y, k_z \in \mathbb{R}, k = \frac{\omega}{c}$	

free-space path loss altogether. The second-row PSF accounts for the spherical spread of the scattered wave only, whereas the PSF in the third row accounts for the spherical spread of both waves, incident and reflected. We note that the amplitude variation of the monostatic-radar waves ($\sim 1/r^2$) over the aperture is not negligible when the measurements are taken with wide-beam antennas and at close range. The close-range scenario occurs when the target range (the depth distance from the acquisition aperture) is comparable to or smaller than the aperture's extent (see Figure 4). We briefly comment that in radar imaging, the close-range scenario is often referred to as *near-field imaging* since the measurements are taken in the near zone of the imaged object. To avoid confusion with the near-field zone of antennas, here, we prefer the term *close-range imaging*. Finally, we note that the choice of PSF from Table 1 has no impact on the speed of the image reconstruction.

Once the PSF $H(\boldsymbol{r}, \omega)$ is chosen and its 2D FT is known, formulating the image-reconstruction formula of DH3D is straightforward. Since DH3D views the imaged object as a collection of uncoupled point scatterers, it models the received scattered signal as a superposition of the contributions from all points making up the object in the imaged volume V':

$$E^{\text{sc}}(x, y, \bar{z}, \omega) = \iiint_{V'} f(x', y', z') H(x - x', y - y', \bar{z} - z', \omega)\, dx' dy' dz'. \tag{3}$$

Here, $f(x', y', z')$ represents the object's reflectivity distribution, whereas $E^{\text{sc}}(x, y, \bar{z}, \omega)$ represents the measured scattered wave over the 2D aperture at $z = \bar{z}$ and at the angular frequency ω. Recognizing the convolution in (x, y) and taking the 2D FT of both sides of (3), leads to

$$\mathcal{F}_{2\text{D}}\{E^{\text{sc}}(x, y, \bar{z}, \omega)\} \equiv \tilde{E}^{\text{sc}}(k_x, k_y, \bar{z}, \omega) = \int_{z'} \tilde{f}(k_x, k_y, z') \tilde{H}(k_x, k_y, \bar{z} - z', \omega) dz' \tag{4}$$

where $\tilde{f}(k_x, k_y, z') = \mathcal{F}_{2\text{D}}\{f(x', y', z')\}$ and $\tilde{H}(k_x, k_y, \bar{z} - z', \omega) = \mathcal{F}_{2\text{D}}\{H(x, y, \bar{z} - z', \omega)\}$. It is now clear that the 2D FT of the PSF, $\tilde{H}(k_x, k_y, \bar{z} - z', \omega)$ (see the second column of Table 1) is critically important for the image reconstruction. All three analytical FTs in Table 1 are in the form $\tilde{H}(k_x, k_y, \bar{z} - z', \omega) = \tilde{h}(k_x, k_y) e^{-\text{i}k_z(\omega)|z' - \bar{z}|}$. This allows for the transformation of (4) into a 3D k-space relation between the unknown target reflectivity $f(x', y', z')$ and the data $E^{\text{sc}}(x, y, \bar{z}, \omega)$. Specifically, assuming that $z' > \bar{z}$, (4) is written as

$$\tilde{E}^{\text{sc}}(k_x, k_y, \bar{z}, \omega) = \tilde{h}(k_x, k_y) e^{\text{i}k_z(\omega)\bar{z}} \int_{z'} \tilde{f}(k_x, k_y, z')\, e^{-\text{i}k_z(\omega)z'} dz'. \tag{5}$$

Since the integral in (5) is a FT with respect to z', (5) is cast in the 3D space of (k_x, k_y, k_z) as

$$\tilde{E}^{\text{sc}}(k_x, k_y, \bar{z}, \omega)[\tilde{h}(k_x, k_y)]^{-1} e^{-\text{i}k_z(\omega)\bar{z}} = \mathcal{F}_{3\text{D}}\{f(x, y, z)\} \tag{6}$$

where $\mathcal{F}_{3\text{D}}\{\cdot\}$ denotes the 3D FT. Note that we have dropped the primed coordinates for the reflectivity function $f(x, y, z)$ since the coordinate system is common for the measurement and imaged points. Finally, the DH3D reconstruction formula is stated as

$$f(x, y, z) = \mathcal{F}_{3\text{D}}^{-1}\left\{\mathcal{F}_{2\text{D}}\{E^{\text{sc}}(x, y, \bar{z}, \omega)\}[\tilde{h}(k_x, k_y)]^{-1} e^{-\text{i}k_z(\omega)\bar{z}}\right\} \tag{7}$$

where $\mathcal{F}_{3\text{D}}^{-1}\{\cdot\}$ is the 3D inverse FT operating on (k_x, k_y, k_z).

For example, in [15] and [21], the PSF in the 2D Fourier space assumes the form $e^{-\text{i}k_z(\omega)|z|}$ (see the first row in Table 1). Thus, $\tilde{h}(k_x, k_y) = 1$, and the reconstruction formula (7) becomes

$$f(x, y, z) = \mathcal{F}_{3\text{D}}^{-1}\{\mathcal{F}_{2\text{D}}\{E^{\text{sc}}(x, y, \bar{z}, \omega_{(k_z)})\} e^{-\text{i}k_z(\omega)\bar{z}}\}. \tag{8}$$

There is one important detail in the implementation of (7) or (8). The 2D FT of the data, $\tilde{E}^{\text{sc}}(k_x, k_y, \bar{z}, \omega) \equiv \mathcal{F}_{2\text{D}}\{E^{\text{sc}}(x, y, \bar{z}, \omega_{(k_z)})\}$, is not an explicit function of k_z; it is a function of ω where the measurements are usually taken at uniform intervals within the frequency bandwidth of the system. In turn, ω is a function of k_z through the dispersion relation in the last row of Table 1. In fact, k_z is not even an independent variable; it is a function of k_x, k_y, and $k = \omega/c$. Thus, the k_z dependence of the data, $\tilde{E}^{\text{sc}}(k_x, k_y, \bar{z}, \omega)$, is implicit through the frequency ω. DH3D deals with this problem by interpolating $\tilde{E}^{\text{sc}}(k_x, k_y, \bar{z}, \omega)$ from the nonuniform $(k_x, k_y, k_z(\omega))$ grid onto a uniform (k_x, k_y, k_z) grid, which allows for the use of FFT algorithms. This operation is called *Stolt interpolation* or *Stolt mapping* [22], and its computational toll is quite significant.

Despite the computational complexity of the Stolt mapping, the DH3D image reconstruction is fast. Figure 5 shows a sample DH3D image of a concealed handgun under clothing. Notice that the image is 2D despite the fact that the reconstruction formula (8) is 3D. The 2D imaging output is common in such systems since it offers faster interpretation, whereas the depth information is not critical for uncovering objects hidden under the clothing. The 2D image is a projection of the 3D object reflectivity onto a single image $I(x, y)$ that depends on x and y only. One possible projection scheme utilizes the expression $I(x, y) = \max_z f(x, y, z)$ [23]. The DH3D imaging systems for personnel inspection are now commercially available and widely used in airports for the security screening of passengers. The images become

available to the security personnel within a second once the measurement is completed.

As mentioned before, the Stolt mapping impacts the speed and accuracy of the DH3D method negatively. This has been the motive behind the development of alternative 3D holographic reconstruction algorithms (discussed in the next section). However, there is an approach that can be still categorized as DH3D but it avoids the Stolt mapping [24]. Therein, the 3D inverse FFT algorithm, which implements the $\mathcal{F}_{3D}^{-1}\{\cdot\}$ operator in (8), is replaced with a sequential application of: 1) nonuniform 1D inverse FFT (NUFFT_{1D}^{-1}) operating on $k_z(\omega)$, and 2) uniform 2D inverse FFT (FFT_{2D}^{-1}) operating on k_x and k_y, i.e.,

$$f(x, y, z) = \text{FFT}_{2D}^{-1}\{\text{NUFFT}_{1D}^{-1}\{\tilde{E}^{sc}(k_x, k_y, \bar{z}, \omega_{(k_z)})\, e^{-ik_z\bar{z}}\}\}. \tag{9}$$

The principles of microwave holography are applicable to cylindrical acquisition surfaces as well (e.g., see [21], [25], [26], [27], [28], and [29]). In particular, the implementation of DH3D for cylindrical whole-body scanners is described in detail in [21].

Spatial Resolution and Sampling Requirements in Imaging With Far-Field Measurements

Far-field measurements provide scattered signals containing only propagating modes since evanescent modes are too weak to be detected. The propagating modes correspond to the real positive k_z values only, as determined from the eigenvalue equation in the last row of Table 1. Figure 6 illustrates the coverage of these modes in the 3D spatial frequency space of k_x, k_y, and k_z when using monostatic radar. This coverage is limited to the $k_z \geq 0$ half-space. Additionally, from the eigenvalue relation $k_x^2 + k_y^2 + k_z^2 = (2k)^2$, it is clear that the coverage is confined within a hemispherical shell. The shell is limited by a hemisphere of radius $2k_{\min}$ from below and a hemisphere of radius $2k_{\max}$ from above, where $k_{\min}$ and $k_{\max}$ are the wavenumbers at the lowest and the highest frequency of operation, respectively. These limits are illustrated in Figure 6(a) and (b), which show cuts in the $k_y = 0$ and $k_z = 0$ planes, respectively. Figure 6(c) shows a cut in the plane $k_z = 2k_c$, where k_c is the wavenumber at the center frequency.

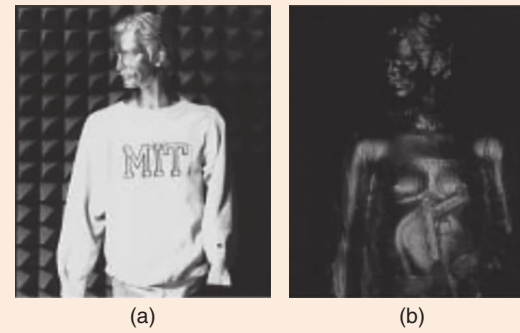

Figure 5. *(a) Optical image and (b) mm-wave image of a clothed mannequin with a concealed Glock-17 handgun. To obtain the mm-wave image, DH3D is used in processing the data in the 100- to 112-GHz frequency band [15].*

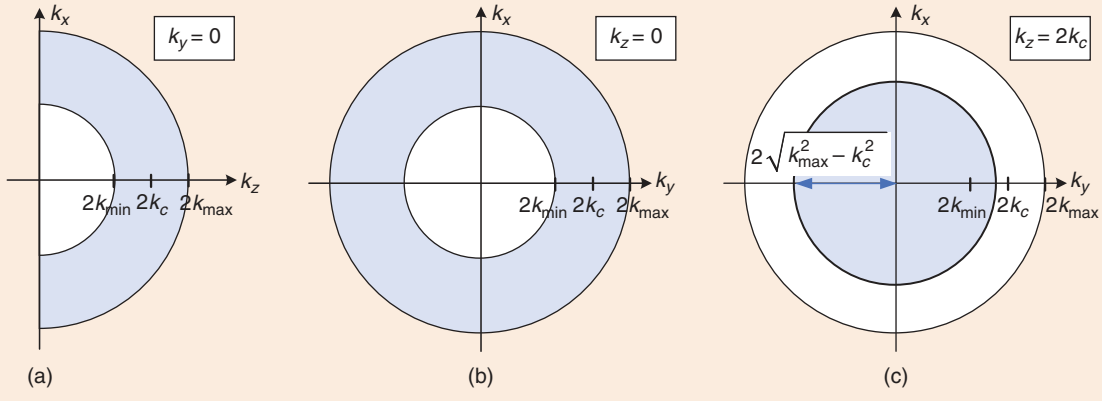

Figure 6. *Illustration of the region spanned by the Fourier variable values (shaded in blue) in the 3D spatial frequency space (k_x, k_y, k_z) when using far-field measurements with a monostatic radar. For simplicity, the illustration does not account for limits imposed by a system's maximum viewing angle $\alpha_{\max} < 90°$. (a) A cut in the $k_y = 0$ plane, where the k_x and k_z variables span one-half of a circular band with an inner radius of $2k_{\min}$ and an outer radius of $2k_{\max}$. Here, $k_{\min}$ and $k_{\max}$ denote the wavenumbers at the minimum and maximum frequency of operation, respectively. The wavenumber corresponding to the center frequency is k_c. (b) A cut in the $k_z = 0$ plane, where the k_x and k_y variables span a circular band of inner radius $2k_{\min}$ and outer radius $2k_{\max}$. (c) A cut in the $k_z = 2k_c$ plane, where the k_x and k_y variables span a circle of radius $2\sqrt{k_{\max}^2 - k_c^2}$.*

The extent of the spectral region of the propagating modes is fundamental in understanding the spatial resolution limits of images obtained from far-field measurements. The image spatial resolution δ_ξ, $\xi \equiv x, y, z$, along the three principal real-space axes, is estimated from the average (over all angles of incidence) span K_ξ along the respective principal Fourier-space axis K_ξ as $\delta_\xi \approx 2\pi/K_\xi$ [3]. Since k_x and k_y span a range from $-2k_c$ to $2k_c$ (on average), the cross-range resolution is estimated as

$$\delta_{x,y} \approx \frac{2\pi}{4k_c} = \frac{\lambda_c}{4} \tag{10}$$

where λ_c is the wavelength at the center frequency of the band. On the other hand, k_z spans a range from $2k_{\min}$ to $2k_{\max}$, leading to an estimated range resolution of

$$\delta_z \approx \frac{2\pi}{2(k_{\max} - k_{\min})} = \frac{c}{2B} \tag{11}$$

where B is the frequency bandwidth of the system.

In practice, the far-field 3D Fourier region is further limited by the maximum viewing angle $\alpha_{\max}$ of the measurement system. This angle equals either one-half of the antenna beamwidth or one-half of the angle defined by the center of the imaged domain and the extremities of the scanned aperture, whichever is smaller. A limited viewing angle ($\alpha_{\max} < 90°$) does not allow for measuring scattered-wave signals arriving at the acquisition aperture at grazing angles, effectively limiting the minimum value of $k_z(k)$ to about $k_{z,\min} \approx 2k\cos\alpha_{\max}$. This result for $k_{z,\min}$ is a consequence of approximating the scattered wave of wavenumber k_0 as a plane wave $\sim \exp(-\mathrm{i}2\boldsymbol{k}_0 \cdot \boldsymbol{r})$, where $\boldsymbol{k}_0 = (k_{x0}, k_{y0}, k_{z0})$ is the wave vector of magnitude $|\boldsymbol{k}_0| = k_0 = \omega_0/c$ and $\boldsymbol{r}$ is the vector from the point of scattering to the measurement point. The 3D FT of this plane wave is a δ-function that peaks at the point $(2k_{x0}, 2k_{y0}, 2k_{z0})$ in Fourier space, i.e., the Fourier variables (k_{x0}, k_{y0}, k_{z0}) are simply the projections of the wave vector $\boldsymbol{k}_0$ onto the x, y, and z axes. Thus, a scattered wave of wavenumber k, which arrives at the aperture at an angle of incidence α, features a Fourier variable $k_z \approx 2k\cos\alpha$. With $\alpha_{\max} < 90°$, $k_{z,\min} \approx 2k\cos\alpha_{\max}$ cannot attain a value of zero, i.e., the measurement of grazing waves is impossible. This in turn sets the upper bound for the Fourier variables k_x and k_y to $(k_x^2 + k_y^2)_{\max} = (2k\sin\alpha_{\max})^2$. Thus, the expression for the cross-range resolution (10) must be corrected as

$$\delta_{x,y} \approx \frac{\lambda_c}{4\sin\alpha_{\max}}. \tag{12}$$

We note that a limited viewing angle has negligible impact on the range resolution δ_z.

The sampling requirements are fundamental in the design of an imaging system, and they stem from understanding its limitations. The spatial sampling steps along the acquisition aperture, Δx and Δy, along with the frequency sampling step Δf employed by all far-field imaging systems, are determined from the Nyquist sampling criterion [3], [15]. Considering the upper bound $2k_{\max}$ for k_x and k_y as discussed above, the spatial sampling requirement is $\Delta x, \Delta y \le \lambda_{\min}/4$, where $\lambda_{\min}$ is the shortest wavelength of the radiation. In practice, oversampling with a step smaller than $\lambda_{\min}/4$ is often detrimental to far-field image reconstruction. This is because the 2D FTs of oversampled scattered signals extend beyond the $2k_{\max}$ limit of the propagating modes and into the evanescent-wave spectrum, where noise prevails. Furthermore, if $\alpha_{\max} < 90°$, the recommended sampling step is corrected to $\Delta x, \Delta y \approx \lambda_{\min}/(4\sin\alpha_{\max})$.

On the other hand, the frequency sampling requirement for monostatic measurements is $\Delta f \le c/(4R_{\max})$, where $R_{\max}$ is the maximum range to target. The maximum range of an imaging radar depends on its transmitted power and its receiver sensitivity. Choosing a sufficiently small Δf prevents range aliasing, i.e., the spurious assignment of the scattering from distant targets to that from closer targets. Similar to spatial sampling, frequency oversampling with Δf much smaller than $c/(4R_{\max})$ may be detrimental in image reconstruction because it associates with scattering beyond $R_{\max}$, where noise and radar clutter prevail.

DH3D-S

As discussed in the previous section, Stolt mapping has a negative impact on the speed and accuracy of the DH3D reconstruction. Here, we describe a category of techniques that avoid Stolt mapping and share one common major characteristic. They all reconstruct the 3D image slice by slice: i.e., the 2D images at each desired range (z) position are reconstructed independently. Like DH3D, they use the far-field PSFs listed in Table 1. We refer to this category of techniques as *DH3D-S*. The main advantage of the DH3D-S methods over DH3D is the improved computational speed.

One DH3D-S approach avoids the Stolt interpolation by using the phase-shift migration (PSM), originally proposed in seismology. In [31], this approach has been applied in the terahertz regime. It employs the PSF shown in the first line in Table 1 along with the plane-wave spectrum range dependence, which predicts that if the scattered field is known at $z = \tilde{z}$, then its 2D FT can be analytically migrated (or backpropagated) along the z-axis and toward the origin of scattering by the phase shift operation

$$\tilde{E}^{\mathrm{sc}}(k_x, k_y, z', \omega) = \tilde{E}^{\mathrm{sc}}(k_x, k_y, \tilde{z}, \omega) e^{\mathrm{i}k_z(z' - \tilde{z})}. \tag{13}$$

In [31] monostatic measurements are considered, where the effective wavenumber is $2k$ since the wave

traverses the distance from the aperture to the target twice. Thus, k_z in (13) is the same as that defined in the last row of Table 1. Note that the range dependence $e^{-ik_z z}$ (in the forward direction) is observed in all PSFs listed in Table 1. Thus, the back-propagation factor $e^{ik_z z}$ holds for the field scattered from a point. Since the scattered response $E^{sc}(x, y, \bar{z}, \omega)$ can be viewed as a superposition of the scattering emanating from all points building the imaged volume, the assumption in (13) that its 2D spectrum $\tilde{E}^{sc}(k_x, k_y, \bar{z}, \omega)$ has the same range dependence is admissible.

The back-propagated 2D spectrum $\tilde{E}^{sc}(k_x, k_y, z', \omega)$ is the k-space 2D map of $E^{sc}(x', y', z', \omega)$ at the desired range slice z'. The intensity of this map is a representation of the strength of the target's reflectivity distribution at z' because the field strength peaks at the location of its source. This is the well-known principle of the classic back-propagation SAR reconstruction approach. In a mathematical sense, the back-propagation scheme is a projection (or inner product) of the measured responses onto the functional space defined by the system PSFs. In [6] it is shown that such reconstruction minimizes the ℓ_2 norm of the error between the measured data and the prediction of the linearized model of scattering.

Since $E^{sc}(x', y', z', \omega)$ is the 2D inverse FT of $\tilde{E}^{sc}(k_x, k_y, z', \omega)$, the relation between the two is

$$E^{sc}(x', y', z', \omega) = \iint_{k_y k_x} \tilde{E}^{sc}(k_x, k_y, z', \omega) e^{i(k_x x' + k_y y')} dk_x dk_y. \tag{14}$$

Substituting (13) into (14) leads to

$$E^{sc}(x', y', z', \omega) == \iint_{k_y k_x} \tilde{E}^{sc}(k_x, k_y, \bar{z}, \omega) e^{ik_z(z' - \bar{z})} e^{i(k_x x' + k_y y')} dk_x dk_y. \tag{15}$$

Finally, averaging (or summation) over all frequencies is employed, resulting in

$$E^{sc}(x', y', z') = \iiint_{\omega k_y k_x} \tilde{E}^{sc}(k_x, k_y, \bar{z}, \omega) e^{ik_z(z' - \bar{z})} e^{i(k_x x + k_y y)} dk_x dk_y d\omega. \tag{16}$$

The image at each z slice is $|E^{sc}(x, y, z)|$. Thus, the slice-by-slice PSM reconstruction formula can be stated as

$$f(x, y, z) \sim E^{sc}(x, y, z) = \mathcal{F}_{2D}^{-1}\left\{ \int_{\omega} \mathcal{F}_{2D}\{E^{sc}(x, y, \bar{z}, \omega)\} e^{ik_z(z - \bar{z})} d\omega \right\}. \tag{17}$$

As in (7), here we have dropped the primed coordinates since the position in the imaged volume uses the same coordinate system as that for the measurements. It is clear from (17) that an image slice at z = const. can be efficiently obtained through the use of direct and inverse 2D FFT algorithms as long as the data $E^{sc}(x, y, \bar{z}, \omega)$ is on a uniform (x, y) grid. Note that the frequency sampling need not be uniform. The Fourier variable k_z is not subject to the inverse FT and it is computed with the dispersion relation in the last row of Table 1.

Figure 7 shows the optical and reconstructed images of a mannequin with a plastic cap gun hidden beneath a T-shirt using a 0.2-THz monostatic heterodyne transceiver with 15-GHz bandwidth and applying the PSM method [31]. The experiments presented in [31] demonstrate ~2-mm cross-range resolution and ~8.8-mm range resolution. This is an excellent spatial-resolution performance as it comes close to the limits mentioned in the "Spatial Resolution and Sampling Requirements in Imaging With Far-Field Measurements" section.

In [32] the DH3D-S technique has been extended to the case of multistatic radar in a fully parallelizable reconstruction algorithm. There, for each range position z, the back-propagated waves received by all of the receivers on a 2D aperture for each transmitter and at each frequency are first computed in 2D (k_x, k_y) space. Similar to (17), the results are summed together, this time over all of the frequencies and all of the transmitters to generate a 2D image at the desired range position z. Since the process for each transmitter and each frequency can be implemented independently, parallel processing is used to expedite the image reconstruction. It has been shown that 256 times improvement in the reconstruction time can be achieved with this technique compared to the conventional backpropagation SAR-based methods, which operate in real (x, y, z) space, while achieving similar image quality.

Range stacking is another DH3D-S imaging algorithm that avoids the Stolt interpolation through a rigorous mathematical transformation of the Fourier variable k_z onto the wavenumber variable $k = \omega/c$ [33]. It has been extended to 3D imaging in [34] and [35]. In range stacking, the DH3D reconstruction formula in (7) is modified by a change of variable from k_z to k. It follows from the dispersion relation $k_z = \sqrt{(2k)^2 - k_x^2 - k_y^2}$ (see the last row in Table 1) that $dk_z = (4k/k_z)dk$. The

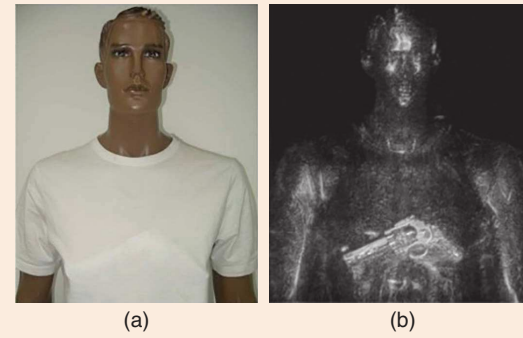

Figure 7. *(a) Optical image of a mannequin with a plastic cap gun beneath a T-shirt. (b) Reconstructed image using the PSM method [31].*

3D inverse FT in (7) can be explicitly stated as a triple integral over k_x, k_y, and k_z:

$$f(x,y,z) = \iiint_{k_z k_y k_x} \mathcal{F}_{2D}\{E^{sc}(x,y,\bar{z},\omega)\}[\tilde{h}(k_x,k_y)]^{-1} \times e^{-ik_z(\omega)\bar{z}} e^{i(k_x x + k_y y + k_z z)} dk_x dk_y dk_z. \quad (18)$$

The change of variable transforms (18) into

$$f(x,y,z) = \iiint_{k_y k_x k} \mathcal{F}_{2D}\{E^{sc}(x,y,\bar{z},k)\} \times \frac{4k e^{i\sqrt{(2k)^2 - k_x^2 - k_y^2}(z-\bar{z})}}{\tilde{h}(k_x,k_y)\sqrt{(2k)^2 - k_x^2 - k_y^2}} e^{i(k_x x + k_y y)} dk\, dk_x dk_y. \quad (19)$$

Note that we have replaced the variable ω with k in $E^{sc}(x,y,\bar{z},k)$ since the simple relation $\omega = k_c$ allows for switching between the two. Finally, the reconstruction formula of the range-stacking algorithm can be stated as

$$f(x,y,z) = \mathcal{F}_{2D}^{-1}\left\{ \int_k \mathcal{F}_{2D}\{E^{sc}(x,y,\bar{z},k)\} \frac{4k e^{i\sqrt{(2k)^2 - k_x^2 - k_y^2}(z-\bar{z})}}{\tilde{h}(k_x,k_y)\sqrt{(2k)^2 - k_x^2 - k_y^2}} dk \right\}. \quad (20)$$

The formula in (20) allows for finding the image at each desired range position $z = \text{const.}$ independently. In [35] the reconstruction formula (20) is employed with the PSF in the second row of Table 1. It is referred to as the *accelerated holographic imaging with LFM* (*AHI-LFM*) since it is applied in an LFM imaging-radar system for whole-body scanning. There, it has been demonstrated that the AHI-LFM algorithm accelerates the image reconstruction by at least an order of magnitude as compared with the DH3D algorithm used previously [23], while preserving the same image quality. Figure 8 shows a volunteer with various hidden items and the reconstructed images using the DH3D and the range-stacking DH3D-S algorithms, confirming similar imaging quality.

In [36] the DH3D-S range-stacking technique has been equipped with compressive-sensing (CS) capability to realize another efficient LFM imaging radar system for whole-body scanning. The reconstruction formula is the same as in (20), where the PSF in the first row of Table 1 is used. Also, the 2D inverse FT is carried out before the integration over k, which is admissible since k_x, k_y, and k are independent variables. The CS algorithm reported in [36] succeeds in producing high-fidelity images with randomly sampled sparse datasets amounting to just 30% of the full datasets, which comply with the Nyquist spatial-sampling recommendation.

DH3D-N

In [37], [38], and [39], direct 3D microwave holography has been extended to near-field imaging where the analytical approximations of the PSF, such as those in Table 1, are inadequate. Instead, simulations are employed to obtain the incident field and Green's function, from which the PSF is then computed. Such PSFs represent better the specific antennas and acquisition setup.

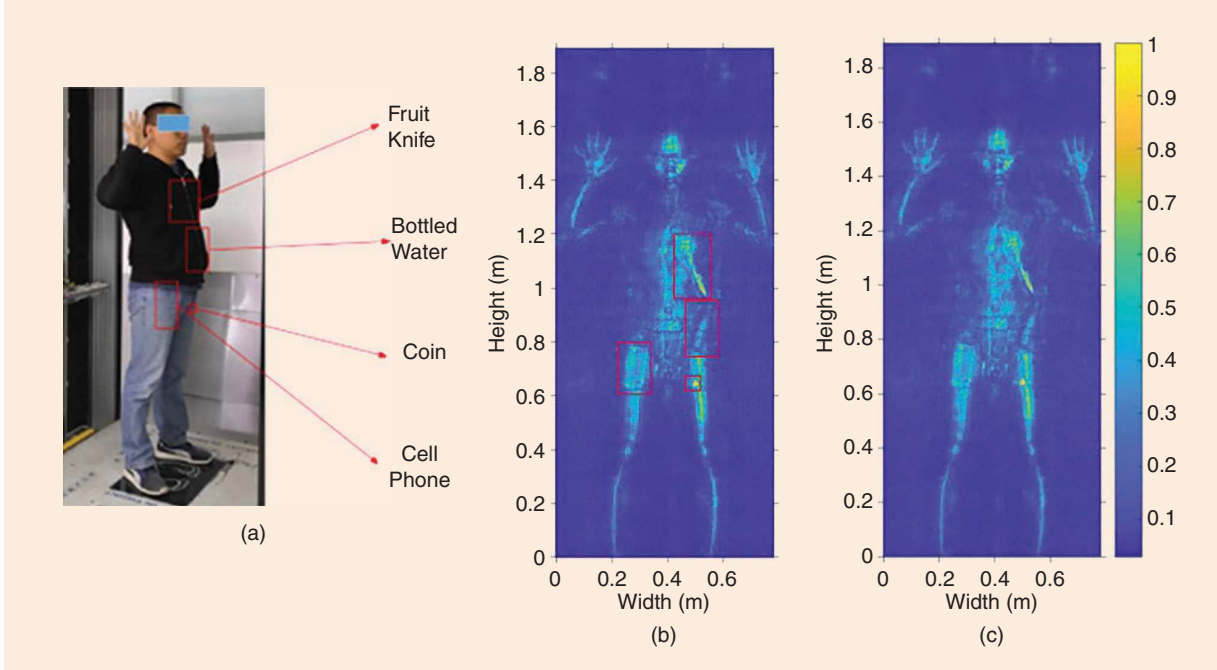

Figure 8. *(a) Optical image of a volunteer with various items hidden under the clothing. Reconstructed images using: (b) DH3D, (c) DH3D-S [35]. While the images are of similar quality, the DH3D-S algorithm is much faster.*

To further improve the near-field imaging output, in [40] a method has been proposed to acquire the PSF function $H(\boldsymbol{r}, \omega)$ in (3) via measurements with a calibration object (CO). The CO consists of a very small object (scattering probe) in the background medium, thus emulating a point scatterer, which provides an impulse input to the imaging system. Figure 9 shows an illustration of the DH3D-N measurement procedure [40] for imaging at N_z depths. To simplify the notations, we assume that the measurement aperture is at $\bar{z} = 0$. First, measurements of the scattered signals over the aperture are acquired when the probe is placed at the center of each desired range slice $(0, 0, z_i)$, $i = 1, \ldots, N_z$, one at a time. These measurements, denoted by $H(x, y, z_i, \omega)$, provide the PSFs of the imaging system at each depth $z = z_i$. Then, similar to the DH3D techniques, the linearized model of scattering in (3) and (4) is employed to recover the object's reflectivity $f(x, y, z)$, which again is assumed to be nondispersive, i.e., independent of ω. However, the integral along z is now discretized into a summation over discrete imaged planes at $z = z_i$, $i = 1, \ldots, N_z$. This allows for writing (4) as

$$\tilde{E}^{\text{sc}}(k_x, k_y, 0, \omega) = \sum_{i=1}^{N_z} \tilde{H}(k_x, k_y, z_i, \omega)\tilde{f}(k_x, k_y, z_i). \tag{21}$$

Note that (21) is a linear equation, which is written at each spatial-frequency point $\boldsymbol{k} = (k_x, k_y)$. Such equation can be written for each frequency ω and for each response (e.g., a reflection or transmission measurement). The coefficients $\tilde{H}(k_x, k_y, z_i, \omega)$ are known by measuring the PSFs a priori and then taking their 2D FTs. The data (or measured responses) $\tilde{E}^{\text{sc}}(k_x, k_y, 0, \omega)$ are also known. The unknowns in (21) are the reflectivity values $\tilde{f}(k_x, k_y, z_i)$ corresponding to the N_z depths. Thus, at least N_z equations are needed to solve (21) as a square or overdetermined linear system of equations at $\boldsymbol{k} = (k_x, k_y)$. Multiple equations are indeed available from measurements at multiple (N_ω) frequencies and/or with various (N_a) pairs of TX/RX antennas that move together to scan the aperture. When data at multiple frequencies and multiple channels are collected, the resulting equations in the form of (21) are stacked in a system of equations solved at each $\boldsymbol{k} = (k_x, k_y)$:

$$\boldsymbol{H}(\boldsymbol{k})\boldsymbol{f}(\boldsymbol{k}) = \boldsymbol{d}(\boldsymbol{k}). \tag{22}$$

The data vector is composed as: $[\boldsymbol{d}(\boldsymbol{k})]^T = [\boldsymbol{d}_1^T(\boldsymbol{k}), \ldots, \boldsymbol{d}_{N_\omega}^T(\boldsymbol{k})]$, where $\boldsymbol{d}_n^T(\boldsymbol{k}) = [\tilde{E}_1^{\text{sc}}(\boldsymbol{k}, 0, \omega_n), \ldots, \tilde{E}_{N_\text{a}}^{\text{sc}}(\boldsymbol{k}, 0, \omega_n)]$, $n = 1, \ldots, N_\omega$. The vector of unknowns is composed as: $\boldsymbol{f}(\boldsymbol{k}) = [\tilde{f}(\boldsymbol{k}, z_1), \ldots, \tilde{f}(\boldsymbol{k}, z_{N_z})]^T$. Accordingly, the system matrix $\boldsymbol{H}(\boldsymbol{k})$ contains the values of the Fourier-transformed PSFs arranged as

$$\boldsymbol{H}(\boldsymbol{k}) = \begin{bmatrix} \boldsymbol{H}_1(\boldsymbol{k}) \\ \vdots \\ \boldsymbol{H}_{N_\omega}(\boldsymbol{k}) \end{bmatrix},$$
$$\boldsymbol{H}_n(\boldsymbol{k}) = \begin{bmatrix} \tilde{H}_1(\boldsymbol{k}, z_1, \omega_n) & \cdots & \tilde{H}_1(\boldsymbol{k}, z_{N_z}, \omega_n) \\ \vdots & \ddots & \vdots \\ \tilde{H}_{N_\text{a}}(\boldsymbol{k}, z_1, \omega_n) & \cdots & \tilde{H}_{N_\text{a}}(\boldsymbol{k}, z_{N_z}, \omega_n) \end{bmatrix}, n = 1, \ldots, N_\omega. \tag{23}$$

The size of $\boldsymbol{H}(\boldsymbol{k})$ is $(N_\omega N_\text{a}) \times N_z$. Thus, (22) is a relatively small linear system of equations since N_ω is on the order of 10 to 100, N_a is on the order of 1 to 4, and N_z is typically 3 to 10.

The solutions of all systems of equations, i.e., for all $\boldsymbol{k} = (k_x, k_y)$, provide the FT of the images $\tilde{f}(k_x, k_y, z_i)$ at each range position $z = z_i$. Two-dimensional inverse FTs applied to each $\tilde{f}(k_x, k_y, z_i)$ generate the slice-by-slice image $f(x, y, z_i)$, $i = 1, \ldots, N_z$.

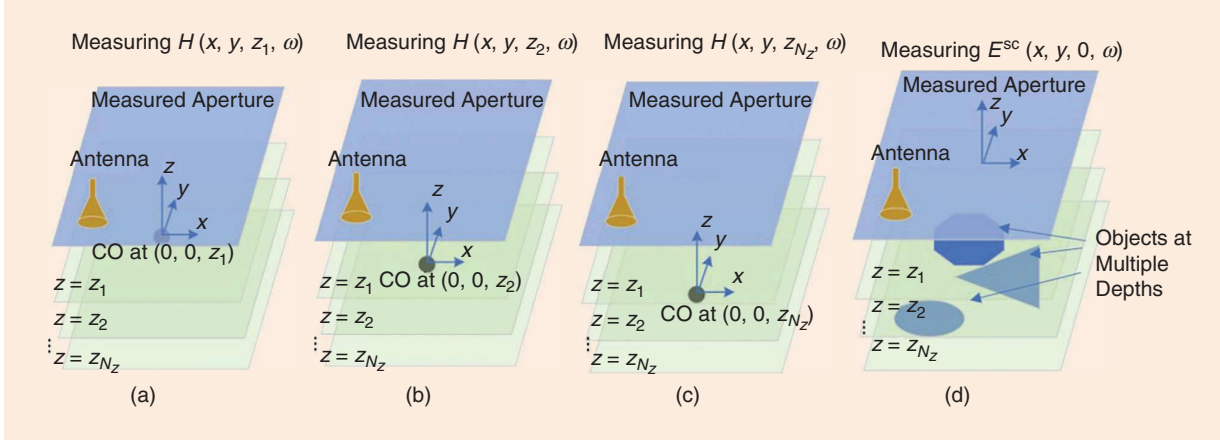

Figure 9. *Illustration of the DH3D-N setup when the aperture is at $\bar{z} = 0$ [40]. The PSFs are measured with the scattering probe (CO) placed at the origin of: (a) first imaged plane at $z = z_1$, providing $H(x, y, z_i, \omega)$, (b) second imaged plane at $z = z_2$, providing $H(x, y, z_i, \omega)$, and (c) N_z-th imaged plane at $z = z_N$, providing $H(x, y, z_i, \omega)$. (d) Measurement of the scattered field due to objects at all imaged depths $z = z_1, .., z_{N_z}$.*

The DH3D-N methods employing measured PSFs offer several advantages over the DH3D and DH3D-S techniques.

- Measured PSFs account for the near-field distribution of the antennas used in the particular imaging setup.
- Measured PSFs provide actual responses, such as S-parameters or voltages, unlike analytical PSFs, which assume that a scalar far-field value is measured at a point. Even if the scattered signal emanates from the far-field region of the RX antenna, the response at its terminals is not proportional to a single vector-field component at the center of its aperture. Antennas respond to the vector-field distribution in their vicinity, not just the aperture center. This "integrating" property of the antenna is ever so important in near-field measurements. Moreover, the way antennas respond to the field depends on frequency.
- Measured PSFs account for the exact properties of the background medium (instead of assuming certain background wavenumber, as is done in the DH3D and DH3D-S techniques). The specific measurement environment is also accounted for, which includes not only the background medium but the components of the imaging setup, such as the antennas, positioner, chamber, etc.
- Measured PSFs capture quantitatively the system sensitivity to the contrast of a point scatterer since the scattering probe in the CO measurement is usually of known material properties and size. This allows for quantitative imaging, briefly discussed later in this section.
- The DH3D-N system of equations solved at each spectral point $\boldsymbol{k} = (k_x, k_y)$ has much smaller dimensions and is less ill-conditioned compared with the systems of equations constructed in the optimization-based quantitative microwave imaging techniques. DH3D-N is not only computationally efficient, but it is also naturally suited for parallel computations because the linear systems of (22) are solved independently at each $\boldsymbol{k} = (k_x, k_y)$.
- The interpolation of the data in k-space (Stolt interpolation) is not necessary in DH3D-N.
- The assumption that k_x, k_y, and k_z are independent variables, which leads to errors in the DH3D image reconstruction, is also unnecessary.
- The data collected by multiple antennas, such as forward-scattered and back-scattered signals, can be easily combined in a single linear system of equations to improve the image spatial resolution and to suppress image artifacts.
- Unlike DH3D, but similarly to DH3D-S, DH3D-N reconstructs the 3D image as a stack of slice images at desired range positions. Unlike DH3D-S, however, all slices are extracted simultaneously leading to faster computations.
- The DH3D-N algorithm can operate with a small number of frequency samples, especially when multiple TX/RX channels are available. This is in contrast to DH3D, where the 3D inverse FT demands dense sampling along k_z, which in turn requires a large number of frequency samples [see (8)].

A comprehensive review of the major developments in DH3D-N can be found in [41]. Here, we only mention that initially, the range resolution of the DH3D-N techniques has been guaranteed by wideband frequency data [37], [38], [39],–[40], similar to the DH3D and DH3D-S techniques. However, it has been shown that a single-frequency multistatic configuration with one TX antenna and an array of RX antennas, both scanning the aperture together, provides sufficient information to achieve range resolution [42]. This offers further advantages, including:

- A single-frequency or narrowband measurement system is more cost-effective, compact and easier to design.
- Resonant antennas can be employed that, in addition to the previous advantage, offer higher sensitivity compared to wideband antennas. This enhance the dynamic range of the imaging system.
- Compact low-cost data-acquisition techniques, such as the modulated scatterer technique [43], can be employed. This allows for using fast electronic scanning instead of the slow mechanical scanning of the sensors over the 2D aperture, paving the way toward real-time imaging applications.
- Although a DH3D-N method has been proposed to take into account the dispersive properties of the object's reflectivity [37], this issue has not been considered widely in direct holography techniques. Neglecting the dispersive material properties can cause additional errors in wideband imaging. This issue is nonexistent in single-frequency systems, and it is negligible in narrowband imaging systems.
- Measurement time is shorter for a single-frequency or narrowband frequency-sweep system. This is important in many applications, such as object tracking or medical imaging, where patient movement during a scan may generate artifacts.

In the far-field systems employing DH3D or DH3D-S, it is assumed that the wavenumber of the background medium is known. In many applications, however, such as nondestructive testing or biomedical imaging, the background wavenumber is not exactly known, which leads to imaging errors. In [44] an algorithm has been presented to estimate the properties of the background medium based on DH3D-N image reconstruction with wideband data. For this purpose, the collected data

(from measuring both the object under test and the system PSF) at multiple frequencies are divided into two sets corresponding to frequencies with even and odd indices. Then, each set is used with several plausible background wavenumbers for image reconstruction. Finally, a cost function, which is the ℓ_2-norm of the difference between the images reconstructed from the two sets for each background wavenumber, is computed. It is shown that the cost function attains a minimum only for the true background medium. In the last step, the data at all frequencies are employed simultaneously with the so obtained background wavenumber to reconstruct the final image.

Recently, in a major step toward fast quantitative microwave imaging suited for biomedical applications, quantitative DH3D-N methods have been presented in [45] and [46]. This is accomplished by measuring the PSF with a scattering probe of known size and permittivity, e.g., a small cylinder (size is less than quarter-wavelength) made of microwave ceramics. According to the linearized scattering model, the measured PSFs, $H_r(x, y, z_i, \omega)$, $r = 1,\ldots,N_a$, $i = 1,\ldots,N_z$, $n = 1,\ldots,N_\omega$, are proportional to the probe's volume Ω_{sp} and relative-permittivity contrast $\Delta\varepsilon_{r,sp}$. This allows for extracting the object's contrast $\Delta\varepsilon_r$ quantitatively by scaling properly the k-space DH3D-N (21) as [45]:

$$\tilde{S}_r^{sc}(k_x, k_y, \omega_n) = \frac{\Omega_v}{\Delta\varepsilon_{r,sp}\Omega_{sp}} \sum_{i=1}^{N_z} \tilde{H}_r(k_x, k_y, z_i, \omega_n)\Delta\varepsilon_r(k_x, k_y, z_i),$$
$$r = 1,\ldots, N_a, n = 1,\ldots, N_\omega. \quad (24)$$

Here, $\tilde{S}_r^{sc}(k_x, k_y, \omega_n)$ is the 2D FT of the scattered-field response (e.g., S-parameter or voltage) acquired with the rth antenna pair at the nth frequency, $\tilde{H}_r(k_x, k_y, z_i, \omega_n)$ is the 2D FT of the PSF measured with the scattering probe of volume Ω_{sp} and relative-permittivity contrast $\Delta\varepsilon_{r,sp}$ positioned at the center of the z_i slice, $\Delta\varepsilon_r(k_x, k_y, z_i)$ is the 2D FT of the object's contrast at the z_i slice, and Ω_v is the volume of a voxel in the 3D image.

Quantitative DH3D-N methods have the potential to make real-time biomedical imaging systems a reality. They offer reconstruction speed that is far superior to the speed of optimization-based quantitative MMI techniques [3], while at the same time achieving comparable image quality. As an example, consider the imaging of a 55-mm-thick compressed breast phantom, which is based on transmission (bistatic) S-parameter measurement [46] with two boresight aligned antennas scanning two parallel planes. The boresight transmission measurement has the advantage of maximum scattered-field strength due to the shortest possible path through the highly dissipative breast-tissue medium. The disadvantage is that the planar boresight arrangement leads to loss of range resolution and the images are only 2D, similar to X-ray mammography. Figure 10 shows the constructed phantom using five 11-mm-thick custom-made carbon-rubber slabs. The custom complex permittivity of these slabs is tailored to match the average permittivity of Breast Imaging Reporting and Data System type 2 breast tissue, which has scattered fibroglandular content of less than 50% of the overall breast-tissue mass. Inside two of the five slabs (slabs 2 and 4), sections are hollowed out and tissue simulants are inserted (see Figure 10(a) and (b). The cancerous tissue simulants are dark in color (circled in blue). The white-colored simulant represents healthy fibroglandular tissue. The brown-colored simulant is that of scattered fibro-glandular tissue and it has permittivity that matches approximately that of the carbon-rubber slabs. All five carbon-rubber slabs are stacked to form the completed phantom [see Figure 10(c)], wherein layers 1, 3, and 5 are homogeneous. Plastic wrap is used to secure the inclusions in layers 2 and 4 as well as to hold together the whole phantom.

First, PSF measurements are performed using a small dielectric cylinder of relative permittivity $\varepsilon_{r,sp} = 50 - i0.05$ (microwave ceramics), of radius 5 mm and height 10 mm as the scattering probe. The scattering probe is embedded

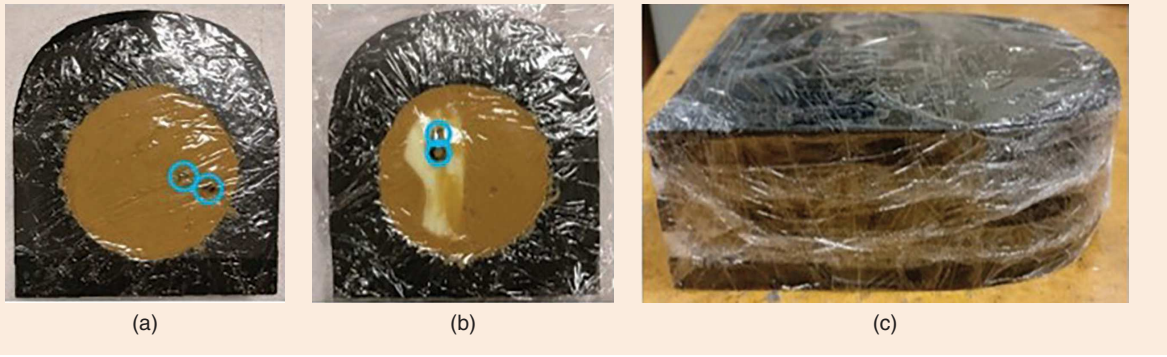

Figure 10. *Photographs of the compressed breast phantom. (a) Layer 2, containing two tumor simulants (circled with solid blue line) in the embedding (brown) medium emulating scattered fibroglandular tissue. (b) Layer 4, containing two tumor simulants (circled with solid blue line) within the fibroglandular simulant (white) in the embedding medium, and (c) assembled phantom [46].*

in the center of a 55-mm-thick stack of five 11-mm-thick uncut homogeneous carbon-rubber slabs.

Solving quantitative (24) provides the images of the real and imaginary parts of the breast phantom shown in Figure 11(a). Due to the lack of range resolution, these are 2D images, which are effectively displaying the object's relative complex-permittivity averaged over the depth of the breast phantom (z-axis). To validate the quantitative accuracy of the reconstruction, Figure 11(b) shows the actual 2D distribution of the averaged real and imaginary relative permittivity.

In [47] the DH3D-N technique of [40] has been extended to cylindrical setups targeting applications in nondestructive testing. The method employs convolution and its efficient computation in k-space, similarly to the rectangular-aperture case. Another similarity is the use of multiple frequencies and/or multiple TX/RX channels to improve the range (radial) resolution. However, there is a difference in processing the data along the azimuthal direction ϕ in a cylindrical setup compared to a rectangular setup, because all of the functions (responses and the contrast function) are periodic along ϕ. As explained in [47], the discrete FT (DFT) accommodates the data periodicity along ϕ, whereas the discrete-time FT (DTFT) is suitable for the data dependence on the vertical (z) position. For the difference between the DFT and DTFT, as well as their implementation, refer to [48]. Similarly to the planar case, a system of equations is constructed and solved for the unknown object reflectivity at each Fourier variable pair (k_ϕ, k_z), where k_ϕ and k_z correspond to the spatial variables ϕ and z, respectively.

An important advantage of the cylindrical setups is that radial resolution can be obtained with narrowband data provided an array of RX antennas is employed to receive the scattered signals due to one or more TX antennas. In [49] one TX antenna and an array of eight RX antennas move together to scan a cylindrical aperture with radius of 60 mm and height of 160 mm, where the envisioned application is biomedical imaging. Due to the narrowband operation, a custom cost-effective data acquisition system for vector measurements is constructed, thus replacing the costly and bulky general-purpose instruments such as vector network analyzers.

In [50] and [51] the cylindrical DH3D-N technique is applied to the nondestructive testing of multiple concentric nonmetallic pipes through imaging of their defects. In [50], wideband data (8 to 12 GHz) are collected to image double concentric pipes. The solution of the system of equations at each spectral point (k_ϕ, k_z) is then augmented using beam-space transformation, which focuses the image on the surface of each pipe and improves the image quality for the pipes that are farther away from the antennas. In contrast, in [51], narrow-band data (or even single-frequency measurement at 10 GHz) are collected by an array of RX antennas distributed along the azimuthal direction on both sides of a TX antenna. The system achieves drastically improved radial resolution compared to the wideband system in [50]. With a similar number of antennas, the method in [51] can image concentric pipes with only 1-mm gap between their walls whereas the method in [50] requires at least an 18-mm gap. Figure 12 shows the nondestructive testing tool reported in [51] along with sample images produced for defects on double concentric polyvinyl chloride pipes using the 10-GHz data only. Figure 13 shows the 1D image cuts through the defects on the double concentric pipes (two defects on the outer pipe and one defect on the inner pipe) for a small gap of only 1 mm between the pipes, demonstrating the striking radial (range) resolution even when using single frequency data at 10 GHz. Achieving high radial resolution in [51] inspired further work, which led to a method to estimate the thickness of defected regions in thick pipes [52].

For DH3D-N techniques, the sampling steps should be smaller than the recommendations discussed in the "Spatial Resolution and Sampling Requirements in Imaging With Far-Field Measurements" section. This is due to the fact that in the near-field measurements, parts of the evanescent wave spectrum can be

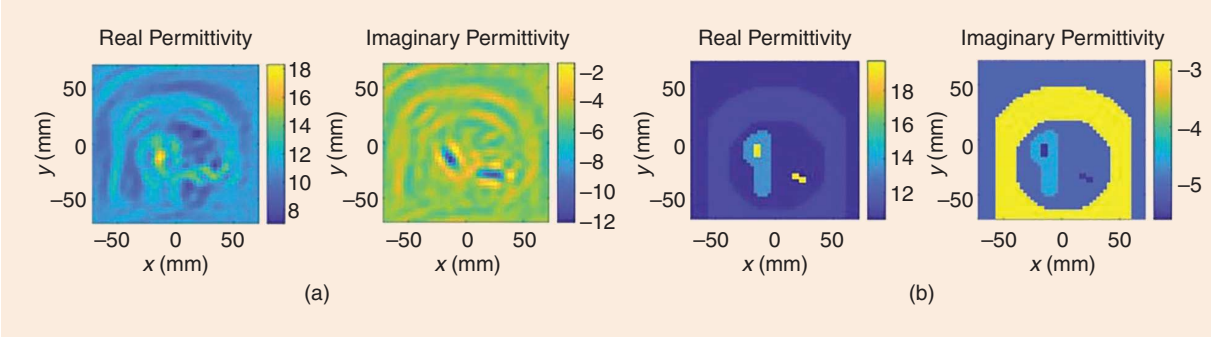

Figure 11. *(a) Two-dimensional quantitative images of the 55-mm compressed breast phantom shown in Figure 10 showing the real and the imaginary parts of the relative permittivity averaged over the phantom's depth. (b) Actual distributions of the real and imaginary relative permittivity when averaged over the depth of the phantom. (From [46].)*

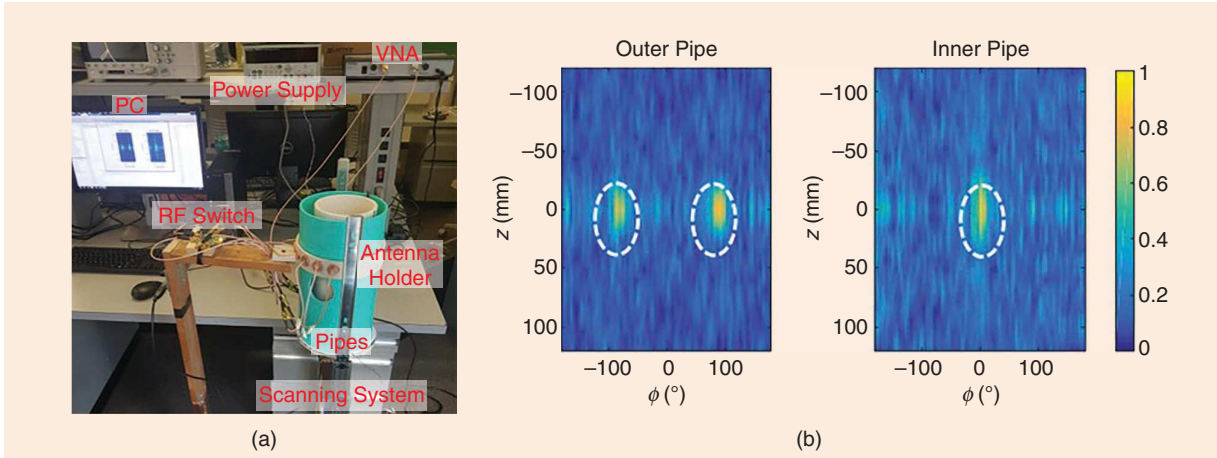

Figure 12. *(a) Experimental setup in [51] for the imaging of double concentric pipes at 10 GHz when the antenna array is placed outside the outer pipe. (b) The imaging results at the surfaces of the outer and the inner pipe, separated by a 1-mm gap. The dashed white lines show the boundaries of the defective regions on the pipes.*

measured over the scanned aperture. This spectrum contains spatial frequency values that lie beyond the $2k_{\max}$ limit as a result of the near-field variations in the spatial (x and y) domain, which are faster than those of the far field. Measurement of these components provides information for larger k_x and k_y values leading to better cross-range resolutions. However, analytical estimates of the maximum limits of k_x and k_y when using near-field measurements do not exist. Thus, these limits must be determined carefully for the DH3D-N techniques. These limits are used to set the width of low-pass filters applied to the reconstructed reflectivity in k-space (before applying inverse FT) in order to suppress erroneous output resulting from excessive noise at the high spatial frequencies [20], [45]. Choosing too large limits may lead to the processing and amplification of high-frequency noise in the images. Furthermore, discontinuities of the responses at the edges of the measurement aperture lead to Gibb's artifacts ("ringing") in the spectral domain, which in turn, causes artifacts in the reconstructed images. This problem is alleviated using apodization filters that damp down the sharp response discontinuities at the edges of the measurement aperture [45].

Progress Toward Real-Time Imaging: Expediting the Recording Step

The holographic imaging techniques discussed earlier in this article are fast. They can provide 3D images of electrically very large scenes within seconds. The computational efficiency benefits from the use of FFT and inverse FFT to implement the direct and inverse FTs. Further acceleration is achieved by parallelizing the computations. For example, in the DH3D-N methods, the systems of equations constructed at each Fourier variable pair—(k_x, k_y) in the rectangular setups or (k_ϕ, k_z) in the cylindrical setups—are independent; thus, they can be solved in parallel, leading to drastic reduction of the running time.

Unfortunately, while holographic image reconstruction techniques are very fast, currently, the data acquisition through 2D scanning on rectangular or cylindrical apertures is slow, hindering the real-time imaging of moving objects. Here, we briefly review the recent advances to address this bottleneck via the use of: 1) the electronic scanning of a 1D antenna array

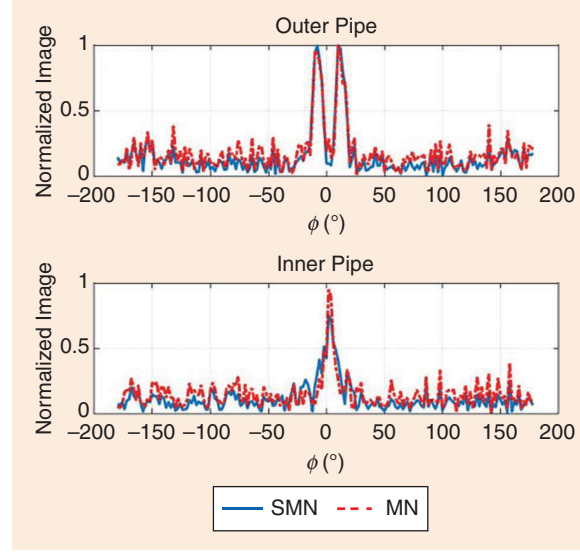

Figure 13. *One-dimensional cuts (along ϕ) of the images of defects on double concentric pipes (two defects on the outer pipe and one defect on the inner pipe) for a gap of 1 mm between the pipe walls [51], where single-frequency measurement at 10 GHz is employed. The DH3D-N systems of equations in k-space are solved with two methods: standardized minimum norm (SMN) and minimum norm (MN), showing reduced artifacts when using the SMN approach.*

and mechanical scanning of the array along a direction perpendicular to the array axis, 2) the electronic scanning of 2D antenna arrays, 3) sparse arrays of TX and RX antennas and collecting data corresponding to the midpoint of the phase centers of each TX/RX pair, 4) stationary MIMO antenna configurations, 5) frequency-modulated continuous wave (FMCW) radar-based data collection, and 6) analytical refocusing of a PSF measured at a certain range position to other range positions when using DH3D-N methods.

The first approach to expedite the data acquisition is electronic scanning with switched antenna arrays, where the antennas are distributed over the measurement aperture. The most common approach is to employ electronic scanning along one direction and mechanical scanning along the other orthogonal direction to cover a 2D aperture. This approach is employed in [15] and [53] for imaging setups paired with DH3D image reconstruction, as well as in [54] and [55] for cylindrical setups with DH3D-N reconstruction. In [56] and [57] a sparse multistatic linear antenna array has been proposed to improve the speed of the measurement and to reduce the complexity of the system. There, the main concept is that a TX/RX antenna pair effectively samples the spatial point located halfway between the phase centers of the two antennas. Thus, using combinations of sparse arrays of TX antennas and RX antennas, dense uniform sampling of the field can be achieved, which emulates a dense virtual transceiver array. This technique substantially reduces the number of antennas and switches while it can result in good imaging performance using the DH3D techniques [15], [21] described earlier.

In [58] the development of a microwave camera is described that operates in the 20- to 30-GHz frequency range. The camera utilizes a 2D array of 16 × 16 elements on a printed circuit board, each operating in a monostatic mode. Each array element consists of a larger tapered-slot TX antenna and two small bow-tie RX antennas located at the edges of the TX slot. The two bow-ties connect to their respective Schottky diodes. The transmitted signal is partially coupled to the two bow-tie antennas, providing the reference signal. The signals reflected by the object are picked by the RX antennas and are mixed with the reference signals by the Schottky diodes. The low-frequency voltages generated by the diodes of the array are multiplexed to two analog-to-digital convertors for sampling. The use of dual receivers provides nonuniform spatial sampling for nonuniform SAR processing, like the approach in [24], which has been discussed above. The camera produces 3D images at a video frame rate of 30 frames per second. Figure 14 shows the schematic of the microwave camera in [58] along with the imaging results for objects hidden inside a laptop bag.

In [59] a fully electronic E-band imager has been presented for high-speed imaging with typical measurement time of 20 ms. It is based on a stationary multistatic array architecture, which employs linear SFCW signal in the 70- to 80-GHz bandwidth. Figure 15 shows the imaging system along with some sample images it produces of a person carrying a P99 pistol hidden underneath clothing. Note that these images are reconstructed with the BPA (see [60]). The BPA, which processes the data directly in real (x, y, z) space, is less computationally efficient than the Fourier-based (holographic) algorithms [60] described here. However, the uniformly sampled data provided by this system can be processed by holographic algorithms.

In [61] another microwave camera with dimensions of 280 mm × 225 mm × 140 mm is reported based on a 2D array of 576 switchable slot antennas operating at 24 GHz. The data collection employs the modulated scattering technique (MST) [43] and the processing is based on a DH3D technique. The use of the MST technique allows for dense sampling (every $\lambda/2$) of the scattered fields by a large number of sampling probes (planar array of 24 × 24 slot antennas). The probes are modulated with a frequency of 1 MHz. The modulated RF outputs of all sampling probes are collected by a network of rectangular waveguides, acting as the MST collector. A heterodyne receiver measures the collector output signals at a fixed intermediate frequency of 10.7 MHz. Figure 16 shows the schematic of the imaging system and an image of a balsa wood sample with a small rubber inclusion. This system provides images with a video frame rate of 22 frames per second. The microwave camera in [58], discussed earlier, offers higher imaging speed and simplicity of the microwave circuitry, compared to the one in [61]. This is due to the use of built-in dual receivers at radiating ends allowing a low-frequency multiplexing network that leads to more compact, efficient, and cost-effective portable system, compared to the one in [61].

The other approach to expedite the data acquisition process is the use of stationary MIMO configurations. In [19] a sparse planar MIMO imaging system has been proposed for fast data collection and the imaging technique belongs to the DH3D category. The array consists of 12 TX and 13 RX antennas arranged along two orthogonal axes, which collect data from 3 to 19.5 GHz. Further, in [62] a highly efficient DH3D algorithm is proposed for MIMO arrays in a cylindrical configuration.

The advancements described so far are based on stepped-frequency measurements. Yet, such measurements are lengthy and the associated hardware is relatively expensive [63]. This is particularly true when enhanced range resolution is desired, which demands wideband data. The alternative offered by FMCW radars

is advantageous due to faster data acquisition while being more cost-effective. Most of the FMCW radar systems proposed so far are based on LFM radars.

In LFM radar, heterodyne mixing provides an intermediate frequency version of the LFM signal. In [23] a rigorous mathematical model of the holography-based imaging with LFM radar is presented, in which system limitations in terms of the object extent and distance are derived and explicitly related to the frequency-modulation slope. The imaging system in [23] is paired with the DH3D image reconstruction, whereas in [35] it employs the DH3D-S method for improved computational speed.

In [64] an LFM radar is paired with a virtual MIMO antenna array. The TX and RX antennas in a sparse MIMO configuration are paired to approximate a monostatic radar operation. In other words, assuming that the distances between the TX and RX antennas in the MIMO array are much smaller than the distance to the target, each TX/RX pair is assumed to represent a transceiver located at the midpoint between them. In [65] a W-band LFM MIMO system is proposed for far-field 3D imaging with BPA-based image reconstruction. In [66] a generalized LFM-based SAR method is proposed, which uses a triangular frequency-modulated waveform to perform 2D imaging.

Finally, despite the advantages highlighted earlier in exploiting measured PSFs in the DH3D-N methods, when the number of imaged slices (N_z) is large,

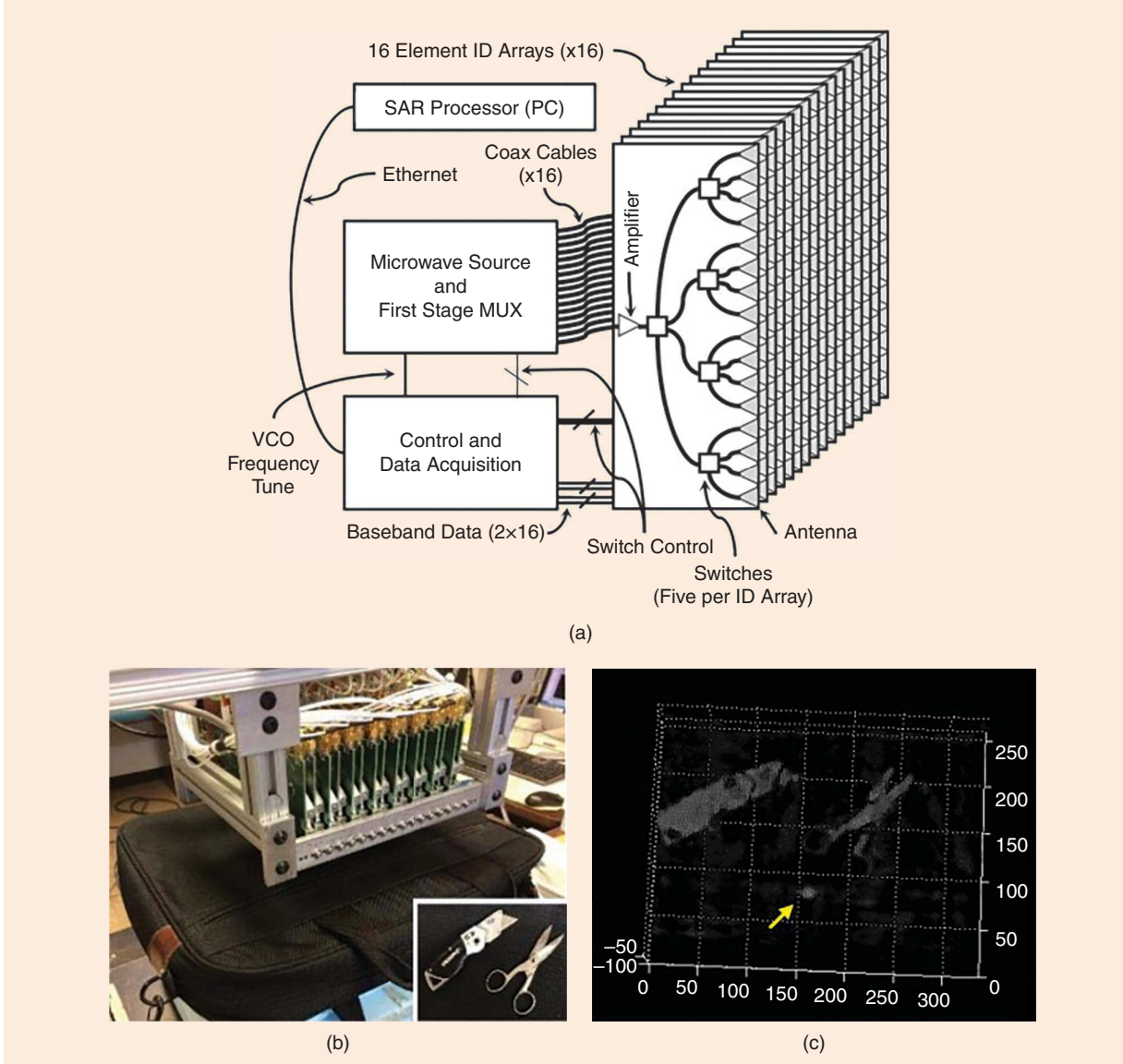

Figure 14. *(a) Schematic of the 3D microwave camera in [58]. (b) Laptop bag placed in front of the camera with inset showing the objects hidden inside the bag. (c) Reconstructed 3D view of the object including a metallic button pointed by the arrow. MUX: multiplexer; VCO: voltage-controlled oscillator.*

the measurement of the PSFs with the scattering probe placed at each imaged slice becomes very time-consuming. To alleviate this practical issue, a method has been proposed in [20] to analytically refocus a measured monostatic PSF with a scattering probe at $z = z_0$, $H(x, y, z_i, \omega)$, to any other range position $z_0 + \Delta z$. The refocusing is done directly in k-space and it employs the range dependence of the PSF in the third line of Table 1, leading to a simple range-migration expression: $\tilde{H}(k_x, k_y, z_0 + \Delta z, \omega) = \tilde{H}(k_x, k_y, z_0, \omega) z_0 e^{-ik_z \Delta z}/(z_0 + \Delta z)$.

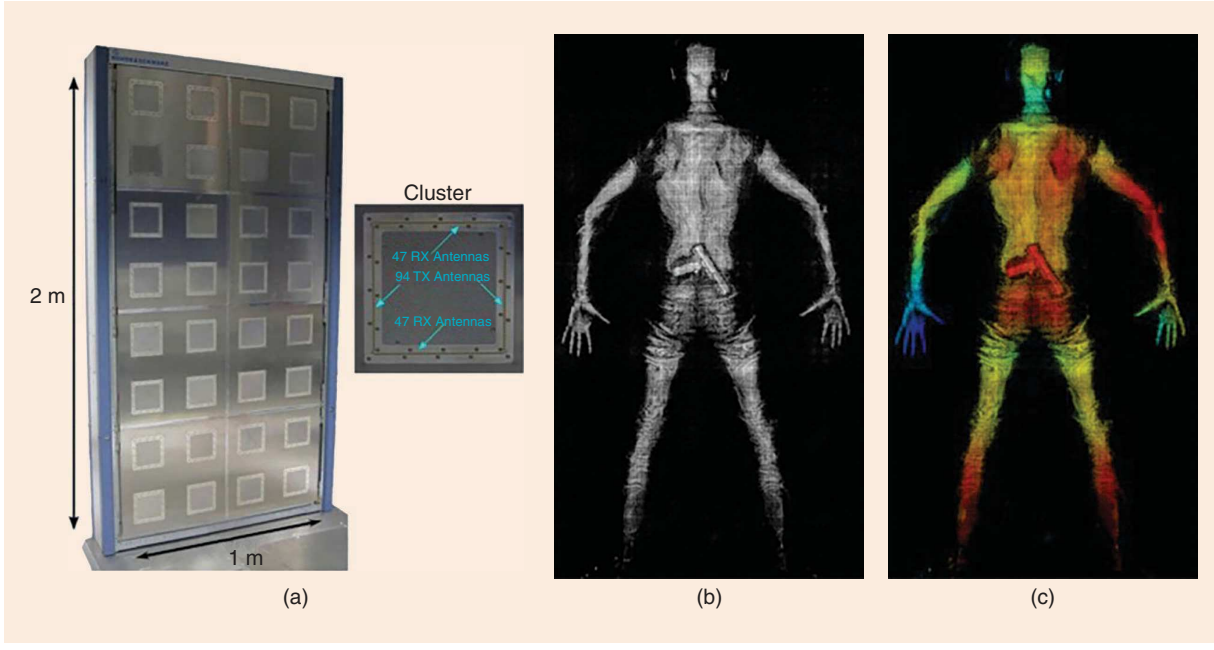

Figure 15. *(a) Personnel imager proposed in [59] with dimensions of 2 m × 1 m, including 32 clusters, each with 94 TX and 94 RX antennas. The reconstructed image of a person concealing a P99 pistol is visualized as: (b) a reflectivity image in logarithmic scale and (c) a color-coded reflectivity image with depth.*

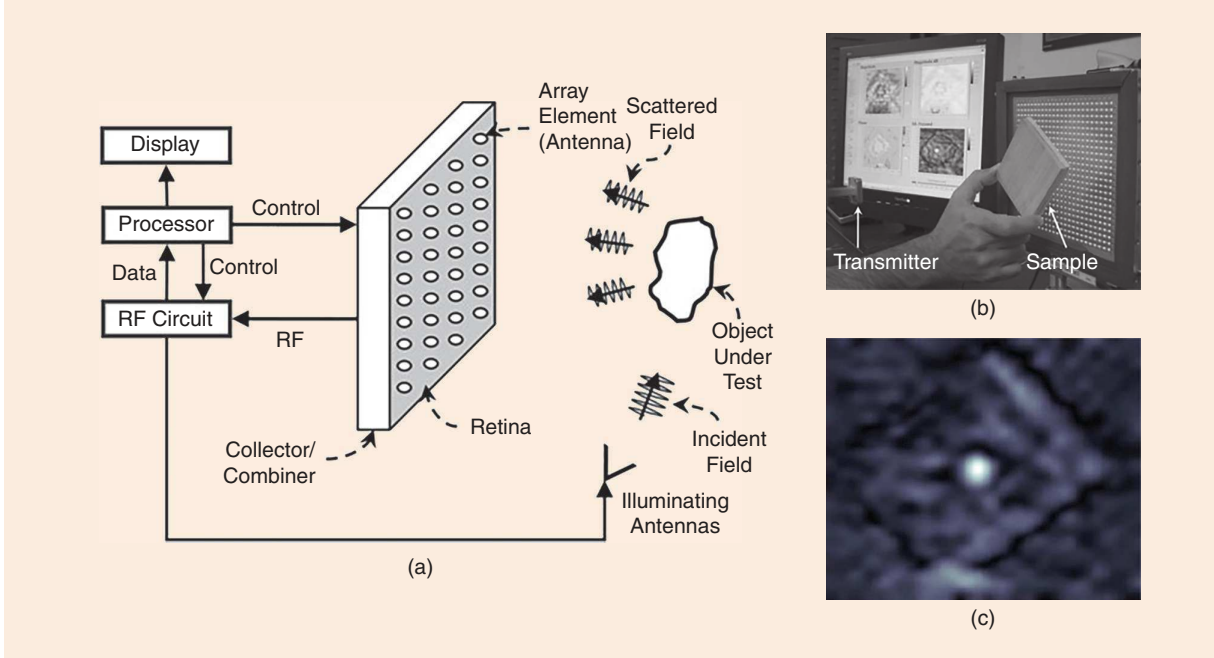

Figure 16. *(a) Schematic of the microwave camera proposed in [61]. (b) Imaging experiment with a balsa wood sample with a small rubber inclusion. (c) Snapshot of reconstructed DH3D image as the sample is being positioned close to the aperture.*

Outlook for Holographic MMI

It has been more than 70 years since the original holographic imaging concepts were proposed by Gabor. Since then, in the microwave and mm-wave regimes, major advancements have been made in data-acquisition schemes, hardware, and processing algorithms. Electronically switched antenna arrays and MIMO systems have opened the pathway toward fast real-time imaging systems capable of producing an image within a second, and often being able to capture objects in motion. With the advent of low-cost chip-scale systems implementing FMCW radars and software-defined radios, building fast microwave and mm-wave imagers is within reach. These technological developments and fast reconstruction algorithms will make microwave and mm-wave video cameras a reality. Deployment of such cameras on mobile platforms will give them a new unique sensing capability, complementing optical and infrared imagery. With its unrivaled speed and resilience to noise and uncertainty, holographic image reconstruction has become the frontrunner toward achieving these goals.

While holographic MMI is best known for the now ubiquitous security screening systems, many other applications are emerging in biomedical imaging and nondestructive testing as briefly discussed here. In such close-range and extreme near-field imaging scenarios, adaptations of microwave holography to near-field applications such as DH3D-N and quantitative microwave holography have been proven to be critical.

Acknowledgment

This work has been supported in part by the by U.S. National Science Foundation, Award 1920098, the Natural Sciences and Engineering Research Council of Canada, Canada Foundation for Innovation, and several New York Institute of Technology's Institutional Support for Research and Creativity grants.

References

[1] D. Gabor, "A new microscope principle," *Nature*, vol. 161, no. 4098, pp. 777–778, 1948, doi: 10.1038/161777a0.

[2] E. N. Leith and J. Upatnieks, "Reconstructed wavefronts and communication theory," *J. Opt. Soc. Amer.*, vol. 52, no. 10, pp. 1123–1130, 1962.

[3] N. K. Nikolova, *Introduction to Microwave Imaging*. Cambridge, U.K.: Springer-Verlag, 2017.

[4] E. J. Feleppa, "Holography and medicine," *IEEE Trans. Biomed. Eng.*, vol. 19, no. 3, pp. 194–205, May 1972, doi: 10.1109/TBME.1972.324117.

[5] B. P. Hildebrand and B. B. B, *An Introduction to Acoustical Holography*. New York, NY, USA: Plenum, 1972.

[6] R. Dooley, "X-band holography," *Proc. IEEE*, vol. 53, no. 11, pp. 1733–1735, Nov. 1965, doi: 10.1109/PROC.1965.4350.

[7] E. N. Leith, "Quasi-holographic techniques in the microwave region," *Proc. IEEE*, vol. 59, no. 9, pp. 1305–1318, Sep. 1971, doi: 10.1109/PROC.1971.8406.

[8] G. Tricoles and N. H. Farhat, "Microwave holography: Applications and techniques," *Proc. IEEE*, vol. 65, no. 1, pp. 108–121, Jan. 1977, doi: 10.1109/PROC.1977.10435.

[9] W. Chew, *Waves and Fields in Inhomogeneous Media*. Piscataway, NJ, USA: IEEE Press, 1995.

[10] D. Smith, O. Yurduseven, B. Livingstone, and V. Schejbal, "Microwave imaging using indirect holographic techniques," *IEEE Antennas Propag. Mag.*, vol. 56, no. 1, pp. 104–117, Feb. 2014, doi: 10.1109/MAP.2014.6821762.

[11] M. Elsdon, O. Yurduseven, and D. Smith, "Early stage breast cancer detection using indirect microwave holography," *Prog. Electromag. Res.*, vol. 143, pp. 405–419, Nov. 2013, doi: 10.2528/PIER13091703.

[12] O. Yurduseven, "Indirect microwave holographic imaging of concealed ordnance for airport security imaging systems," *Prog. Electromag. Res.*, vol. 146, pp. 7–13, Apr. 2014, doi: 10.2528/PIER14032304.

[13] C. Cafforio, C. Prati, and E. Rocca, "SAR data focusing using seismic migration techniques," *IEEE Trans. Aerosp. Electron. Syst.*, vol. 27, no. 2, pp. 194–207, Mar. 1991, doi: 10.1109/7.78293.

[14] D. M. Sheen et al., "Real-time wideband cylindrical holographic surveillance system," U.S. Patent 5,859,609, Jan. 1999 (filed Sep. 1996).

[15] D. M. Sheen, D. L. McMakin, and T. E. Hall, "Three-dimensional millimeter-wave imaging for concealed weapon detection," *IEEE Trans. Microw. Theory Tech*, vol. 49, no. 9, pp. 1581–1592, Sep. 2001, doi: 10.1109/22.942570.

[16] J. M. Lopez-Sanchez and J. Fortuny-Guasch, "3-D radar imaging using range migration techniques," *IEEE Trans. Antennas Propag.*, vol. 48, no. 5, pp. 728–737, May 2000, doi: 10.1109/8.855491.

[17] J. T. Case, M. T. Ghasr, and R. Zoughi, "Optimum two-dimensional uniform spatial sampling for microwave SAR-based NDE imaging systems," *IEEE Trans. Instrum. Meas.*, vol. 60, no. 12, pp. 3805–3815, Dec. 2011, doi: 10.1109/TIM.2011.2169177.

[18] M. Ravan, R. K. Amineh, and N. K. Nikolova, "Two-dimensional near-field microwave holography," *Inverse Problems*, vol. 26, no. 5, 2010, Art. no. 055011, doi: 10.1088/0266-5611/26/5/055011.

[19] X. Zhuge and A. G. Yarovoy, "Three-dimensional near-field MIMO array imaging using range migration techniques," *IEEE Trans. Image Process.*, vol. 21, no. 6, pp. 3026–3033, Jun. 2012, doi: 10.1109/TIP.2012.2188036.

[20] D. Tajik, R. Kazemivala, J. Nguyen, and N. K. Nikolova, "Accurate range migration for fast quantitative Fourier-based image reconstruction with monostatic radar," *IEEE Trans. Microw. Theory Techn.*, vol. 70, no. 9, pp. 4273–4283, Sep. 2022, doi: 10.1109/TMTT.2022.3187090.

[21] D. M. Sheen, D. McMakin, and T. E. Hall, "Near-field three-dimensional radar imaging techniques and applications," *Appl. Opt.*, vol. 49, no. 19, pp. E83–E93, 2010, doi: 10.1364/AO.49.000E83.

[22] R. Stolt, "Migration by Fourier transform techniques," *Geophysics*, vol. 43, no. 1, pp. 49–76, 1978, doi: 10.1190/1.1440826.

[23] Y. Meng, C. Lin, J. Zang, A. Qing, and N. K. Nikolova, "General theory of holographic inversion with linear frequency modulation radar and its application to whole-body security scanning," *IEEE Trans. Microw. Theory Techn.*, vol. 68, no. 11, pp. 4694–4705, Nov. 2020, doi: 10.1109/TMTT.2020.3016323.

[24] J. T. Case, M. T. Ghasr, and R. Zoughi, "Nonuniform manual scanning for rapid microwave nondestructive evaluation imaging," *IEEE Trans. Instrum. Meas.*, vol. 62, no. 5, pp. 1250–1258, May 2013, doi: 10.1109/TIM.2012.2220034.

[25] A. Dallinger, S. Schelkshorn, and J. Detlefsen, "Efficient ω-k-algorithm for circular SAR and cylindrical reconstruction areas," *Adv. Radio Sci.*, vol. 4, pp. 85–91, Sep. 2006, doi: 10.5194/ars-4-85-2006.

[26] J. Detlefsen, A. Dallinger, and S. Schelkshorn, "Effective reconstruction approaches to millimeter-wave imaging of humans," in *Proc. 28th General Assembly Int. Union Radio Sci.*, 2005, pp. 23–29.

[27] W. Tan, W. Hong, Y. Wang, and Y. Wu, "A novel spherical-wave three-dimensional imaging algorithm for microwave cylindrical scanning geometries," *Prog. Electromagn. Res.*, vol. 111, pp. 43–70, Nov. 2011, doi: 10.2528/PIER10100307.

[28] X.-x Meng, S. Wu, T. Li, and H.-k Zhang, "Circular SAR cylindrical area reconstruction using omega-k algorithm based on NUFFT," in *Proc. IEEE 9th U.K.-Europe-China Workshop Millimetre Waves Terahertz Technol. (UCMMT)*, 2016, pp. 215–218, doi: 10.1109/UCMMT.2016.7874016.

[29] B. Ren, S. Li, H. Sun, W. Hu, and X. Lv, "Modified cylindrical holographic algorithm for three-dimensional millimeter-wave imaging," *Prog. Electromag. Res*, vol. 128, pp. 519–537, 2012.

[30] I. Walterscheid, A. Brenner, and J. Ender, "Results on bistatic synthetic aperture radar," *Electron. Lett.*, vol. 40, no. 19, pp. 1224–1225, 2004.
[31] S. Gu, C. Li, X. Gao, Z. Sun, and G. Fang, "Three-dimensional image reconstruction of targets under the illumination of terahertz Gaussian beam — Theory and experiment," *IEEE Trans. Geosci. Remote Sens.*, vol. 51, no. 4, pp. 2241–2249, Apr. 2013, doi: 10.1109/TGRS.2012.2209892.
[32] M. Abbasi, A. Shayei, M. Shabany, and Z. Kavehvash, "Fast Fourier-based implementation of synthetic aperture radar algorithm for multistatic imaging system," *IEEE Trans. Instrum. Meas.*, vol. 68, no. 9, pp. 3339–3349, Sep. 2019, doi: 10.1109/TIM.2018.2875769.
[33] M. Soumekh, "Range stacking: An interpolation-free SAR reconstruction algorithm," *Proc. SPIE*, vol. 3370, pp. 13–24, Sep. 1998, doi: 10.1117/12.321823.
[34] W. Tan, P. Huang, Z. Huang, Y. Qi, and W. Wang, "Three-dimensional microwave imaging for concealed weapon detection using range stacking technique," *Int. J. Antennas Propag.*, vol. 2017, Aug. 2017, Art. no. 1480623, doi: 10.1155/2017/1480623.
[35] Y. Meng, C. Lin, A. Qing, and N. K. Nikolova, "Accelerated holographic imaging with range stacking for linear frequency modulation radar," *IEEE Trans. Microw. Theory Techn.*, vol. 70, no. 3, pp. 1630–1638, Mar. 2022, doi: 10.1109/TMTT.2021.3136292.
[36] S. Li, G. Zhao, H. Sun, and M. Amin, "Compressive sensing imaging of 3-D object by a holographic algorithm," *IEEE Trans. Antennas Propag.*, vol. 66, no. 12, pp. 7295–7304, Dec. 2018, doi: 10.1109/TAP.2018.2869660.
[37] R. K. Amineh, M. Ravan, A. Khalatpour, and N. K. Nikolova, "Three-dimensional near-field microwave holography using reflected and transmitted signals," *IEEE Trans. Antennas Propag.*, vol. 59, no. 12, pp. 4777––4789, Dec. 2011, doi: 10.1109/TAP.2011.2165496.
[38] R. K. Amineh, A. Khalatpour, H. Xu, Y. Baskharoun, and N. Nikolova, "Three-dimensional near-field microwave holography for tissue imaging," *Int. J. Biomed. Imag.*, vol. 2012, Apr. 2012, Art. no. 291494, doi: 10.1155/2012/291494.
[39] R. K. Amineh, M. Ravan, J. McCombe, and N. K. Nikolova, "Three-dimensional microwave holographic imaging employing forward-scattered waves only," *Int. J. Antennas Propag.*, vol. 2013, Aug. 2013, Art. no. 897287, doi: 10.1155/2013/897287.
[40] R. K. Amineh, J. McCombe, A. Khalatpour, and N. K. Nikolova, "Microwave holography using point-spread functions measured with calibration objects," *IEEE Trans. Instrum Meas.*, vol. 64, no. 2, pp. 403–417, Feb. 2015, doi: 10.1109/TIM.2014.2347652.
[41] R. K. Amineh, N. K. Nikolova, and M. Ravan, *Real-Time Three-Dimensional Imaging of Dielectric Bodies Using Microwave/Millimeter Wave Holography*. Hoboken, NJ, USA: Wiley, 2019.
[42] R. K. Amineh, M. Ravan, R. Sharma, and S. Baua, "Three-dimensional holographic imaging using single frequency microwave data," *Int. J. Antennas Propag.*, vol. 2018, Jul. 2018, Art. no. 6542518, doi: 10.1155/2018/6542518.
[43] J.-C. Bolomey and F. Gardiol, *Engineering Applications of the Modulated Scatterer Technique*. Norwood, MA, USA: Artech House, 2001.
[44] H. Wu, K. Patel, and R. K. Amineh, "Quality enhancement in holographic imaging by background property estimation," *IEEE Trans. Antennas Propag.*, vol. 68, no. 7, pp. 5748–5752, Jul. 2020, doi: 10.1109/TAP.2020.2963916.
[45] D. Tajik, A. D. Pitcher, and N. K. Nikolova, "Comparative study of the Rytov and Born approximations in quantitative microwave holography," *Prog. Electromag. Res. B*, vol. 79, pp. 1–19, 2017.
[46] D. Tajik, R. Kazemivala, and N. K. Nikolova, "Real-time imaging with simultaneous use of Born and Rytov approximations in quantitative microwave holography," *IEEE Trans. Microw. Theory Techn.*, vol. 70, no. 3, pp. 1896–1909, Mar. 2022, doi: 10.1109/TMTT.2021.3131227.
[47] R. K. Amineh, M. Ravan, H. Wu, and A. Kasturi, "Three-dimensional holographic imaging using data collected over cylindrical apertures," *Microw. Opt. Technol. Lett.*, vol. 61, no. 4, pp. 907–911, 2019, doi: 10.1002/mop.31694.
[48] A. V. Oppenheim, R. W. Schafer, and J. R. Buck, *Discrete-Time Signal Processing*. 2nd ed. Upper Saddle River, NJ, USA: Prentice Hall, 1999.
[49] H. Wu and R. K. Amineh, "A low-cost and compact three-dimensional microwave holographic imaging system," *Electronics*, vol. 8, no. 9, 2019, Art. no. 1036, doi: 10.3390/electronics8091036.
[50] R. K. Amineh, M. Ravan, and R. Sharma, "Nondestructive testing of nonmetallic pipes using wideband microwave measurements," *IEEE Trans. Microw. Theory Techn.*, vol. 65, no. 5, pp. 1763–1772, May 2020, doi: 10.1109/TMTT.2020.2969382.
[51] H. Wu, M. Ravan, R. Sharma, J. Patel, and R. K. Amineh, "Microwave holographic imaging of nonmetallic concentric pipes," *IEEE Trans. Instrum. Meas.*, vol. 69, no. 10, pp. 7594–7605, Oct. 2020, doi: 10.1109/TIM.2020.2980340.
[52] M. Shah, Y. Gao, M. Ravan, and R. K. Amineh, "Quantitative defect size evaluation in fluid-carrying nonmetallic pipes," *IEEE Trans. Microw. Theory Techn.*, vol. 70, no. 8, pp. 4071–4081, Aug. 2022, doi: 10.1109/TMTT.2022.3176904.
[53] D. Sheen, D. McMakin, and T. E. Hall, "Cylindrical millimeter-wave imaging technique for concealed weapon detection," in *Proc. SPIE, Int. Soc. Opt. Eng.*, Mar. 1998, vol. 3240, pp. 242–250, doi: 10.1117/12.300061.
[54] H. Wu, M. Ravan, and R. K. Amineh, "Holographic near-field microwave imaging with antenna arrays in a cylindrical setup," *IEEE Trans. Microw. Theory Techn.*, vol. 69, no. 1, pp. 418–430, Jan. 2021, doi: 10.1109/TMTT.2020.3031897.
[55] Y. Gao, M. Ravan, and R. K. Amineh, "Fast, robust, and low-cost microwave imaging of multiple non-metallic pipes," *Electronics*, vol. 10, no. 15, 2021, Art. no. 1762, doi: 10.3390/electronics10151762.
[56] D. M. Sheen, "Sparse multi-static arrays for near-field millimeter-wave imaging," in *Proc. IEEE Global Conf. Signal Inf. Process.*, 2013, pp. 699–702, doi: 10.1109/GlobalSIP.2013.6736987.
[57] D. M. Sheen and T. E. Hall, "Reconstruction techniques for sparse multistatic linear array microwave imaging," in *Proc. SPIE Passive Active Millimeter-Wave Imag.*, 2014, vol. 9078, Art. no. 90780I, doi: 10.1117/12.2053814.
[58] M. T. Ghasr, M. J. Horst, M. R. Dvorsky, and R. Zoughi, "Wideband microwave camera for real-time 3-D imaging," *IEEE Trans. Antennas Propag.*, vol. 65, no. 1, pp. 258–268, Jan. 2017, doi: 10.1109/TAP.2016.2630598.
[59] S. S. Ahmed, A. Genghammer, A. Schiessl, and L.-P. Schmidt, "Fully electronic E-band personnel imager of 2 m^2 aperture based on a multistatic architecture," *IEEE Trans. Microw. Theory Techn.*, vol. 61, no. 1, pp. 651–657, Jan. 2013, doi: 10.1109/TMTT.2012.2228221.
[60] G. Wang, F. Qi, Z. Liu, C. Liu, C. Xing, and W. Ning, "Comparison between back projection algorithm and range migration algorithm in terahertz imaging," *IEEE Access*, vol. 8, pp. 18,772–18,777, 2020, doi: 10.1109/ACCESS.2020.2968085.
[61] M. T. Ghasr, M. A. Abou-Khousa, S. Kharkovsky, R. Zoughi, and D. Pommerenke, "Portable real-time microwave camera at 24 GHz," *IEEE Trans. Antennas Propag*, vol. 60, no. 2, pp. 1114–1125, Feb. 2012, doi: 10.1109/TAP.2011.2173145.
[62] J. Gao, B. Deng, Y. Qin, H. Wang, and X. Li, "An efficient algorithm for MIMO cylindrical millimeter-wave holographic 3-D imaging," *IEEE Trans. Microw. Theory Techn.*, vol. 66, no. 11, pp. 5065–5074, Nov. 2018, doi: 10.1109/TMTT.2018.2859269.
[63] J. Li, H. Wang, X. Wang, Y. Yan, and H. Donglin, "Comparative study on stepped frequency pulsed and continuous wave SARs," *Radar Sci. Technol.*, vol. 14, no. 1, pp. 45–53, 2016.
[64] M. E. Yanik and M. Torlak, "Near-field MIMO-SAR millimeter-wave imaging with sparsely sampled aperture data," *IEEE Access*, vol. 7, pp. 31,801–31,819, 2019, doi: 10.1109/ACCESS.2019.2902859.
[65] D. Bleh et al., "*W*-band time-domain multiplexing FMCW MIMO radar for far-field 3-D imaging," *IEEE Trans. Microw. Theory Techn.*, vol. 65, no. 9, pp. 3474–3484, Sep. 2017, doi: 10.1109/TMTT.2017.2661742.
[66] Y. Nan, X. Huang, and Y. J. Guo, "A millimeter-wave GCW-SAR based on Deramp-on-Receive and piecewise constant Doppler imaging," *IEEE Trans. Geosci. Remote Sens.*, vol. 58, no. 1, pp. 680–690, Jan. 2020, doi: 10.1109/TGRS.2019.2939004.